Original Research

Baptiste Dafflon*
Susan S. Hubbard
Craig Ulrich
John E. Peterson

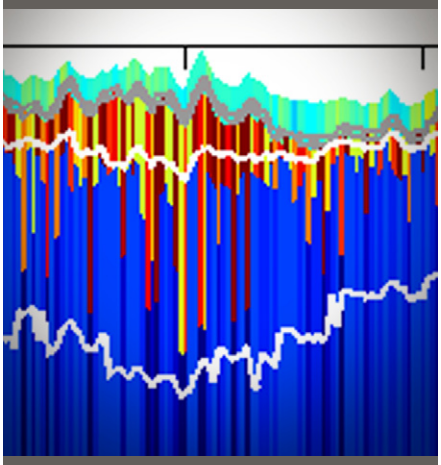

A novel approach has been developed to estimate the subsurface electrical conductivity distribution from electromagnetic induction data and evaluate influence of prior constraints, data information content, and solution non-uniqueness. Its application to an Arctic ecosystem enabled imaging of the variability of active layer and permafrost properties.

B. Dafflon, S.S. Hubbard, C. Ulrich, and J.E. Peterson, Lawrence Berkeley National Lab. (LBNL), 1 Cyclotron Rd., Berkeley, CA 94720. *Corresponding author (bdafflon@lbl.gov).

Vadose Zone J.
doi:10.2136/vzj2012.0161
Received 26 Oct. 2012.

© Soil Science Society of America
5585 Guilford Rd., Madison, WI 53711 USA.
All rights reserved. No part of this periodical may be reproduced or transmitted in any form or by any means, electronic or mechanical, including photocopying, recording, or any information storage and retrieval system, without permission in writing from the publisher.

Electrical Conductivity Imaging of Active Layer and Permafrost in an Arctic Ecosystem, through Advanced Inversion of Electromagnetic Induction Data

Characterizing the spatial variability of active layer and permafrost properties is critical for parameterizing process-rich models that simulate feedbacks from Arctic ecosystem to a changing climate. Because of the sensitivity of electrical conductivity (EC) measurements to moisture content, salinity, and freeze state and the ease of collecting electromagnetic induction (EMI) data with portable tools (e.g., EM38, GEM2, or DUALEM) over large regions, EMI surveys hold great potential for Arctic ecosystem characterization. However, estimation of subsurface EC distribution from such data is challenging because of the insufficient amount of information such data provide towards finding a unique solution. The non-uniqueness problem is often approached by fixing inversion constraints and initial models without a clear understanding of their possible effects on the obtained results. Here we developed a direct search method, which involves a grid-based evaluation of one-dimensional layered model parameters, to estimate EC distribution from EMI data and evaluate the influence of prior constraints, data information content, and solution non-uniqueness. We applied the new method to EMI data acquired in Barrow, AK, as part of the Department of Energy Next-Generation Ecosystem Experiments (DOE NGEE–Arctic). Results demonstrate the success of the developed approach for estimating models that reproduce recorded data within a specified range of uncertainty at each measurement location, as well as the value of different types of constraints. Importantly, the method can be used to quickly investigate the need for and effects of different priors at numerous measurement locations, since the time-consuming simulation of the EMI signals from the multidimensional search grid is performed only once.

Abbreviations: DOE NGEE–Arctic, Department of Energy Next-Generation Ecosystem Experiments; EC, electrical conductivity; EMI, electromagnetic induction; ERT, electrical resistance tomography; MCMC, Markov chain Monte Carlo.

The spatial distribution of soil EC is important in the earth sciences because of its relation to soil properties such as porosity, mineralogy, moisture, and fluid ionic strength (e.g., Archie, 1945; Revil et al., 1998; Friedman, 2005). Electromagnetic induction responses are generated by EC variations (e.g., Everett and Meju, 2005), and thus EMI is widely used for subsurface investigations (e.g., Pellerin, 2002; Auken et al., 2006; Everett, 2012). In comparison to electrical methods, EMI methods do not require contact with the ground and thus can be acquired relatively quickly using airborne or ground survey modes. In summary, with the EMI method, the response of the EC distribution in the subsurface is measured using a combination of two coils. The transmitter coil is energized with alternating current, creating a magnetic field that induces electric currents in the subsurface conductive layers. The currents create a secondary magnetic field, which is shifted in phase with respect to the primary field; both the primary and secondary fields are measured by the receiver coil. Different depth sensitivity functions are obtained using multiconfigurations of the instrument that vary coil spacing, orientation, elevation above ground surface, and signal frequency.

For near-surface investigations, one-person-operated frequency domain EMI instruments (such as EM38, GEM2, and DUALEM) are commonly used for mapping the apparent EC and for estimating soil salinity (e.g., Lesch et al., 1995; Corwin and Lesch, 2005; Quinn et al., 2010), extent of groundwater contamination (e.g., Triantafilis et al., 2011), soil water content (e.g., Reedy and Scanlon, 2003; Robinson et al., 2012), clay content (e.g., Triantafilis and Lesch, 2005), soil characterization (e.g., Abdu et al., 2008; André et

al., 2012; Heil and Schmidhalter, 2012), and wedge locations in polygonal networks (e.g., Cockx et al., 2006; Singleton et al., 2010). Several field studies involving electrical and/or electromagnetic measurements have shown the potential for characterizing the EC distribution within a permafrost system (e.g., Hoekstra et al., 1975; Yoshikawa et al., 2004; Hauck and Kneisel, 2008; Minsley et al., 2012a; Overduin et al., 2012).

Several studies have reported EC values of permafrost systems using electrical or EMI methods. Unconsolidated deposits (such as, e.g., silty sand or fluvial gravel) that are partly or fully saturated with fresh water have been generally reported with EC values above 2 mS/m (<500 Ωm) in unfrozen states and below ~2.9 mS/m (>350 Ωm) in frozen states (e.g., Hoekstra et al., 1975; Hauck and Kneisel, 2008; Minsley et al., 2012a). An exception to this occurs with the presence of clays, which can lead to values as high as 100 mS/m (as low as about 10 Ωm) when unfrozen (e.g., Minsley et al., 2012a) and as high as 20 mS/m (as low as 50 Ωm) when frozen. The presence of saline water, which strongly increases the EC of the sediments and lowers its freezing point, can lead to EC values ranging between 50 and 125 mS/m (8 and 20 Ωm), as observed near Barrow, AK (Yoshikawa et al., 2004), or even as high as 1000 mS/m (1 Ωm) (Overduin et al., 2012). When frozen, saline permafrost regions have led to EC values as high as 50 mS/m (as low as 20 Ωm, e.g., Overduin et al., 2012). The EC values discussed here are only indicative and should not be considered as fixed boundaries between different permafrost lithologies or fluid states.

One reason for the extensive and successful use of portable EMI tools for permafrost and other near-surface investigations is that the coil spacing is much smaller than the skin depth (e.g., McNeill, 1980). As such, the tools are assumed to operate at a low induction number, which permits approximations and simplifications (e.g., McNeill, 1980) in Maxwell's equations that govern electromagnetic theory (e.g., Keller and Frischknecht, 1966). On the basis of this, the apparent EC value can be directly inferred from the measured ratio between the amplitude of the out-of-phase (quadrature) component and the in-phase component of the signal, which is assumed to be equal to the primary field. This apparent EC is defined by the average EC associated with variable subsurface layers included in the EMI measurement support volume, weighted by their relative thickness and their contribution to the signal, which depends on the tool and acquisition configuration (e.g., McNeill, 1980; Everett and Meju, 2005). High EC values and their variations have a stronger influence on EMI measurements compared with low values. Under conditions of low induction number and for simple evaluations, the above approximations are very useful. However, a Maxwell-based full solution is preferable for inversion purposes because it is more reliable, especially when EMI data are being used to characterize heterogeneous environments in the presence of high EC material (e.g., Callegary et al., 2007; Lavoue et al., 2010).

Various approaches have recently been developed to estimate EC from EMI data, including a smooth one-dimensional inversion approach (e.g., Farquharson, 2000; Hendrickx et al., 2002; Huang and Won, 2003; Minsley et al., 2012b), a similar approach that uses lateral constraints along a two-dimensional profile (e.g., Monteiro Santos, 2004; Triantafilis and Monteiro Santos, 2009; Monteiro Santos et al., 2011), and smooth two-dimensional inversion approaches (e.g., Mitsuhata et al., 2006). Recent developments have also trended toward exploring multiple solutions of EC from EMI data instead of only a single best fitting model. Examples include a two-layer, one-dimensional inversion method based on a direct search approach that couples a global and local optimization (Mester et al., 2011) and a one-dimensional layered model estimation based on a Markov chain Monte Carlo (MCMC) approach (e.g., Minsley, 2011; Minsley et al., 2012a).

A common but critical issue with near-surface EMI imaging using data collected with portable tools is the strong non-uniqueness in the solution that is caused by many factors. First, the limited number of measurements can lead to an underdetermined problem, where a unique estimation of the multiple parameters is not possible. Second, the sensitivity function of each of the measurements to the subsurface EC distribution may be not diverse enough to ideally constrain the domain of solution. Finally, EMI and electrical methods face the equivalence problem, meaning that various combinations of layers having different thicknesses and EC values can lead to the same response or measurement (e.g., Keller and Frischknecht, 1966; Koefoed, 1979; Sharma and Kaikkonen, 1999). As a result, the use of various priors, such as inversion constraints and start models, can significantly influence the inversion results (e.g., Hubbard et al., 2013). In summary, although priors and their influence on the inversion process greatly affect the inversion results, because of the limited data information content and the equivalence concern they are rarely quantified (e.g., Sharma and Kaikkonen, 1999; Kafri and Goldman, 2005; Minsley, 2011).

The non-uniqueness limitations described above motivated our study. In particular, we developed a parameter-estimation approach that permits investigation of the information contained in EMI data, the diverse models that reproduce the measured data within a specific range of uncertainty, and the influence of priors on the inversion result. This development is particularly important because inversion of EMI data potentially contains valuable information about the subsurface even if the solution is non-unique. In addition, the obtained information can be used to guide choices about additional measurements and/or prior information needed to improve subsurface characterization or process understanding.

Here we invoked a grid-based direct search parameter-estimation approach, which was a simple method that was particularly adapted to meet our stated objectives. Our study is described as follows: In Section 2, we introduce the grid-search-based approach, and in Section 3, we apply it to datasets collected near Barrow,

AK. The investigations at this site are part of the DOE NGEE–Arctic project that aims to develop a process-rich ecosystem model to simulate the evolution of the Arctic ecosystem in a changing climate. This effort requires the characterization and monitoring of properties and processes from the bedrock to the top of the vegetative canopy—ideally in high resolution, over large spatial scales, and in a minimally invasive manner. The EMI measurements that have been acquired at our study site using a portable tool (as described in Hubbard et al., 2013) require inversion to characterize the EC of the active layer. Inversion of these measurements using a one-dimensional regularized least-squares-based inversion code EM1DFM (Farquharson, 2000) also requires the use of a specific initial model to obtain a realistic result, as will be discussed in Section 3. The parameter-estimation method described here enables investigation of the information content of such data, the non-uniqueness in models reproducing the data, and the influence of prior constraints. In Sections 4 and 5, we discuss the implementation and results, respectively, of our developed method to improve the inversion, and in Section 6 we summarize the findings of our study.

Grid-Search-Based Parameter-Estimation Approach

Grid-search-based approaches involve setting up a multidimensional parameter grid, computing the forward simulation for each combination of parameter values, and evaluating a misfit function to assess how each of them reproduces the measurements (e.g., Sen and Stoffa, 1995; Tarantola, 2005). The grid-search-based workflow of the approach used in this study is shown in Fig. 1. The first step consists of defining a range of EC and thickness values for each of the layers defining a one-dimensional subsurface model and simulating the EMI signals corresponding to the used tool configurations for each combination of parameter values. Because the method simulates the entire search domain without optimization, it is generally considered a computationally intensive parameter-estimation method (e.g., Sen and Stoffa, 1995; Tarantola, 2005) and a viable approach only for the investigation of a limited number of parameters. In this study, the evaluation of several one-dimensional three-layered models was performed by sampling various EC values for each layer and variable thicknesses for the top and middle layer, while the bottom layer was considered to be infinitely thick. The second step of our approach consists of applying prior constraints and discarding a subset of models, both based on site-specific knowledge. Finally, the third and last step involves an evaluation of the misfit between each simulated and measured data pair and the selection of the corresponding models that reproduce the measured data within a given range of uncertainty. These data are then subject to further statistical analysis.

One main advantage of this approach is that the second and third steps are computationally inexpensive, and thus many factors can be considered with minimal computational effort, including

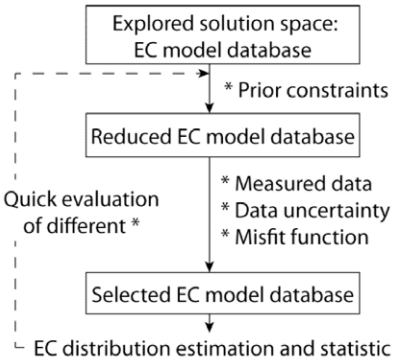

Fig. 1. Workflow of the grid-based parameter-estimation approach for improved evaluation of the influence of various parameterization, priors, and datasets on the inferred subsurface models.

numerous locations (even at various sites), multiple priors, different data uncertainty, and multiple misfit functions. This computationally efficient characteristic of this new approach distinguishes it from other parameter-estimation methods that also seek to explore multiple models, including the direct search approach that couples global and local optimization (Mester et al., 2011) and the MCMC-based approach (Minsley, 2011), both of which require complete or partial simulations at each new measurement location because of their iterative optimization processes. Other characteristics of the method described here include (i) the absence of critical issues that often plague inversion approaches, such as convergence, optimization, regularization, or linearization; (ii) the ability to detect several minimum in the domain of solution, and (iii) the requirement of a simple parallelization on a computer network or cluster to simulate the initial EMI forward simulations (the first step in the procedure).

Field Data

Study Site and Measurements

The study site is located within the Barrow Environmental Observatory (BEO) near the village of Barrow on the Alaskan Arctic Coastal Plain, which is bordered on the north by the Arctic Ocean and on the south by the foothills of the Brooks Range. The landscape of the region has low topographic relief, includes a mosaic of thaw lakes and drained basins (Sellmann et al., 1975; Hinkel et al., 2003; Frohn et al., 2005), and is dominated by different types of polygons (e.g., Hinkel et al., 2001; Hubbard et al., 2013). The shallow subsurface consists of a thin (<1 m) active layer (e.g., Shiklomanov et al., 2010; Goswami et al., 2011) underlain by a permafrost containing frozen soil, ice wedges, and ground ice (e.g., Leffingwell, 1915). The presence of high salinity and partially unfrozen soil in the permafrost zone has been noted by several investigators in the region of Barrow but at variable depths (e.g., Brown, 1969; Yoshikawa et al., 2004; Meyer et al., 2010).

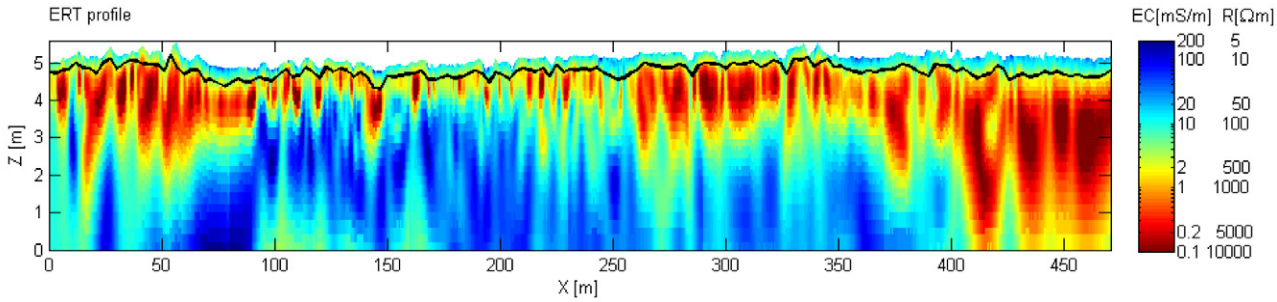

Fig. 2. Electrical resistance tomography (ERT) profile acquired along the centerline and collocated with the electromagnetic induction data. The black line (4.5–5 m) shows the base of the active layer measured with a tile probe (modified from Hubbard et al., 2013). Elevations (Z) in this and subsequent figures are given relative to mean sea level.

The land surface footprint of the investigated zone is a grid that is ~475 m long in SE–NW direction and 40 m wide, which was defined to encompass three different types of ice wedge polygons (i.e., high-centered, low-centered, and transitional). These polygonal landscapes formed through successive freeze–thaw cycles and their geomorphic expressions are related to the integrity of underlying ice wedges (e.g., Leffingwell, 1915). Various geophysical and point measurements, including the EMI data grid, were collected the week of 24 September to 1 October 2011, as described by Hubbard et al. (2013). This time period represents the end of the growing season and the beginning of freeze-up. At the time of EMI data acquisition, some water was visible on the ground surface in polygon troughs, especially at the NW end of the profile, where ~30 cm thick ponds were common. Although during this campaign the surface waters transitioned from thawed to a partially frozen state during the acquisition, the active layer remained unfrozen.

This study focuses on the 475-m-long centerline of the grid, where we take advantage of the highest amount of information. This includes EMI data (discussed below), an electrical resistance tomography (ERT) transect (Fig. 2), and active layer thickness measurements, which were collected every 3 m with a tile probe labeled with centimeter gradations. Details about the ERT and active layer probe measurements are provided in Hubbard et al. (2013).

Electromagnetic Induction Dataset

The EMI data were collected with a EM38-MK2 (e.g., McNeill, 1980; Geonics, 2009) operating at a frequency of 14,500 Hz and with two different transmitter receiver coil separations (1 and 0.5 m). The EMI sensitivity curves calculated using the low induction value approximation (e.g., McNeill, 1980) indicate that in vertical mode with 1-m coil spacing, the signal is most sensitive to EC variations that occur at 0.4 m below ground surface; variations below 0.2 m but above 2 m from ground surface contribute to 75% of the EC response. When collecting in horizontal mode with a 1-m coil separation, the contribution from near-surface material is large and decreases almost monotonically with depth, leading to ~75% response contribution from the zone above 1-m depth (McNeill, 1980). In the case where the coils separation is half (0.5 m), the contribution depths described above are approximately half. It is important to note the ~25% of the response coming from below a given depth can still strongly influence the measured apparent EC, particularly in the case of strong EC contrasts and increasing EC values with depth (e.g., McNeill, 1980; Everett and Meju, 2005).

Acquisition of EMI data at the study site was performed twice using both horizontal and vertical coil orientation modes; each dataset was collected by foot with the instrument located ~0.1 and ~0.05 m above ground surface in vertical and horizontal mode, respectively. An external control unit allowed automatic and synchronized acquisition with positioning using a GPS. Standard tool adjustment was performed at the beginning of each day using the instrument protocol (Geonics, 2009). This procedure involves lifting the instrument 1.5 m high above the ground surface, zeroing the in-phase measurement, and correcting the apparent EC reading if necessary to ensure that the measured value in horizontal configuration is equal to half the value measured in vertical configuration (an assumption based on the design of the tool following McNeill, 1980). In fact, such adjustments and measurements were performed multiple times at a single location (at 154 m along the profile) during the campaign. The maximum shift observed between the mean of all the measurements (obtained from multiple times adjustments) and an individual one was equal to −1 and +1 mS/m for the 1- and 0.5-m coil spacing, respectively. These values are consistent with the correction performed in the adjustment protocol (i.e., involving constant shift in both horizontal and vertical configuration for each coils spacing) but potentially contribute to the uncertainty in the data.

Initial processing of the data consisted of applying a constant shift to the measured apparent EC values to obtain at the adjustment location (at 154 m) the mean values inferred from the multiple adjustments at this location. This required a constant shift equal to −0.5 and +0.5 mS/m for the 1- and 0.5-m coil spacing, respectively. Although we are confident in the adjustment protocol and measured values, we recognize that EMI data can often require

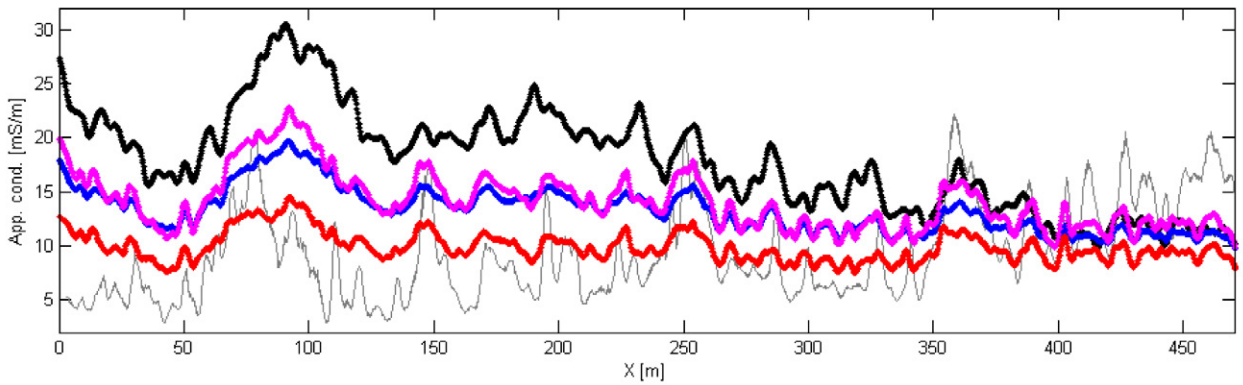

Fig. 3. EM38 data after PCA filtering, including data collected along the centerline using 1-m coil spacing in vertical (black) and horizontal (pink) configuration and 0.5-m coil spacing in vertical (blue) and horizontal configuration (red). The grey line shows the top-layer averaged EC values obtained from the electrical resistance tomography data shown in Fig. 2.

additional adjustments, depending on the time-varying influence of field parameters (temperature, solar radiation) and/or tool particularities (e.g., manufacturer calibration, drift, power supply). To compensate for these additional influences, other studies have shifted the measured values by a constant amount to find a subsurface model that best reproduces the data (e.g., Singleton et al., 2010) or have rescaled the measured values to reproduce the simulations of electromagnetic signals from a collocated ERT profile (e.g., Lavoue et al., 2010; Minsley et al., 2012b). Although the simulation of the EMI signal from a collocated ERT profile does not reproduce the measured EMI signals very well in our study, we chose not to "calibrate" the EMI data with ERT data. We made this choice because the highly heterogeneous subsurface nature of our field study site, which exhibits EC variations over several orders of magnitude (perhaps the greatest range that can be expected), can variably affect EMI and ERT responses, owing to their differences in acquisition, theory, physical processes, and processing.

Further, to preserve the part of the data that is most likely not related to incoherent noise in the various measurement configurations, we attenuated incoherent noise in the data by performing a principal component analysis (PCA) based filtering that has already been successfully used on EMI data by Minsley et al. (2012b). This approach involves singular value decomposition of a matrix containing all the normalized measured signals and then reconstruction of the signals using only a subset of the so-obtained eigenvectors, thus conserving only the information that is most highly correlated between the various signals. Here the PCA analysis showed that for each of the four EMI measured signals, more than 95% of the variability of each signal could be reproduced using the two first eigenvectors, and thus less than 5% by the third and fourth eigenvectors. In an attempt to remove the high frequency incoherent noise that is strongly present in the third and fourth eigenvectors, we reconstructed the four EMI signals using the two first eigenvectors only.

Figure 3 shows the EMI apparent EC values obtained using data measured with 1- and 0.5-m coil spacing in both vertical and horizontal configuration along the centerline after PCA filtering. The apparent EC values range between 7 and ~32 mS/m on the left (south) side and between 8 and ~15 mS/m on the far right (north) side. Importantly, although the apparent EC is lowest on the right site of the profile, this is the region where ponds with standing water are common. Also, the measurements related to largest investigation depth (1-m coil spacing in vertical configuration) shows the highest apparent EC values. These observations indicate that the measured EMI signals are strongly influenced by contributions from the shallow, unfrozen active layer and further by deeper permafrost that contain necessarily a conductive zone to yield the higher apparent EC measured with the 1-m coil spacing in vertical direction. These findings were corroborated by the ERT profile (Fig. 2), which suggest a three-layer system involving a very thin active layer of moderate EC, underlain by a variably thick resistive layer that is in turn underlain by a very conductive zone. The influence of the deeper permafrost and conductive zone influence on the apparent EC derived from the EMI data (even that measured with 0.5-m coils spacing in horizontal direction) is evident by comparing the EMI-obtained EC with the EC obtained from the top 0.2 m in ERT profile (Fig. 3).

Compared with the ERT data (Fig. 2), the EMI data contain much more limited information about the subsurface. Thus, although the influence of a deeper conductive layer is clear in the EMI apparent EC data (Fig. 3), numerous subsurface models can represent such features and reproduce the observed EMI data. This is evident in Fig. 4, which shows models obtained with one-dimensional regularized least-squares-based inversions of the EMI data using EM1DFM (Farquharson, 2000). The inversions differ in the starting model used (i.e., the thickness and the initial EC value assigned to each layer of the model). The inversions yielded dramatically different results, even though they all show a final mean relative misfit between measured and calculated EMI signals smaller than 2.5%. This demonstrates the importance of exploring the non-uniqueness in solution and optimal use of priors.

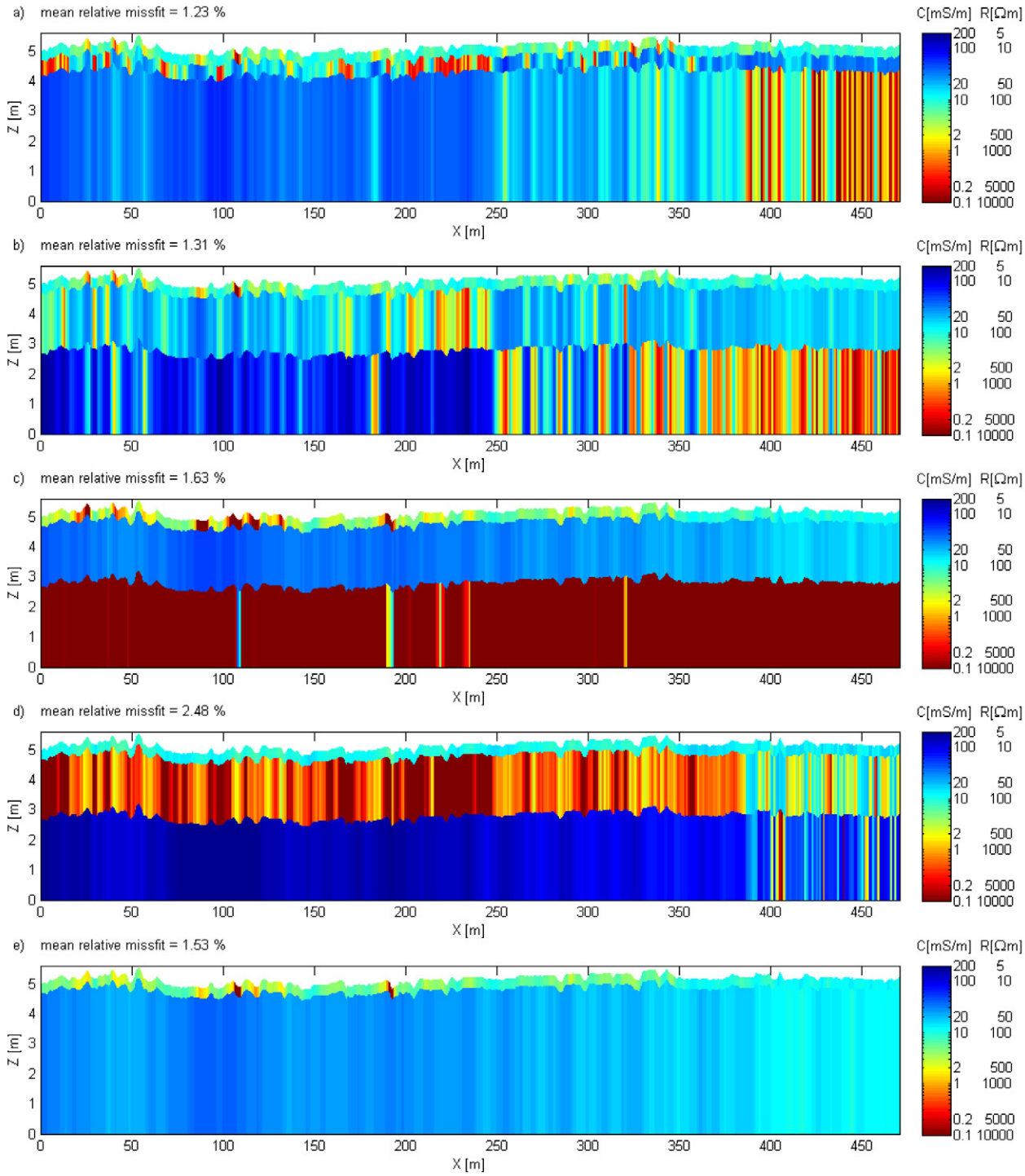

Fig. 4. (a–e) Examples of models obtained with traditional one-dimensional regularized least-squares-based inversions of the electromagnetic induction (EMI) data, which have been all performed with various choices about the fixed layer thicknesses and the initial layer EC values. Although the inversions yield dramatically different results, they all show a final mean relative misfit between measured and calculated EMI signals smaller than 2.5%.

Grid-Search Parameterization

The parameter-estimation described in "Grid-Search-Based Parameter-Estimation Approach" was performed at each measurement location along the EMI transect to identify three-layer models that lead to an acceptable misfit between simulated and measured data. We chose to investigate three-layer models because of: (i) the site-specific knowledge of at least two key layers, including an active layer underlain by variable permafrost; (ii) the observation of three layers from the ERT results; and (iii) the pragmatism of a three-layer model: it includes all the one- and

two-layer models, while many near-surface environments can be characterized to a first order with three layers or less (e.g., Huang and Won, 2003; Triantafilis and Monteiro Santos, 2009; Mester et al., 2011). We are aware that this choice implies that the number of estimated parameters (five) is larger than the number of measurements (four), which means that ours is an underdetermined problem. However, as discussed in the introduction, our main objective here was not to optimize a model to obtain a minimal misfit between calculated and measured data but instead to investigate very diverse subsurface EC distributions that reproduce the measured data within a given range of uncertainty.

In this study, the multiparameter grid search approach samples (for each of the three layers) 36 different possible EC values ranging from 10,000 to 0.025 mS/m (or 0.1 to 40,000 Ωm) that have been obtained by linearly spacing 24 values between 1.6021 and 4 log10 mS/m and replacing the 5 values between 1.7267 and 0.4276 log10 mS/m with 17 linearly spaced values to create a finer grid in this interval. This discretization leads to 36 different EC values for each layer, with a higher sampling rate in the intervals that represent typical EC values for saturated unconsolidated sediments. Further, the top layer was defined with 10 different thickness values from 0.1 to 1 m with 0.1-m increment. The middle layer was defined with 24 different thickness values from 0.1 to 1 m with 0.1-m increment, 1.25 to 2 m with 0.25-m increment, 2.5 to 4 m with 0.5-m increment, and 5 to 10 m with 1-m increment. The bottom layer was considered to be of infinite thickness. For each of the 11,197,440 models created using the above-defined multiparameter grid, the EMI responses were simulated for the EM38 configurations used in the field.

As a quality control measure, the forward EMI simulations were performed using two codes: em1dfmfwd, which was developed at the University of British Columbia (Farquharson, 2000) and em1d, developed at Lawrence Berkeley National Laboratory (e.g., Brown et al., 2012). Both are based on the full solution to Maxwell's equations (e.g., Keller and Frischknecht, 1966; Ward and Hohmann, 1987; Farquharson, 2000) and allow the calculation of the secondary H-field normalized by the primary (i.e., free-space) field for any combination of measurements. These measurements can be made at different frequencies of the transmitter current and for any transmitter and receiver loop separations, orientation, and height above the earth's surface. Very similar results were obtained for both codes, with a mean difference of 0.005% and a maximum difference of 0.1%. For each, the computation of ~11 million simulations took less than 1.5 d on a 16-processor (of 2 cores each) computer (Intel Xeon CPU X5550 at 2.67GHz and 48 GB RAM) and was expected to take less than 1 wk on a standard desktop computer (Intel Core I7 CPU at 2.93 GHz and 8 GB RAM). Although another alternative for performing the forward simulations is to use the low induction number approximation (e.g., McNeill, 1980), which would be about 100 times faster, note that such an approximation is not valid for heterogeneous models (e.g., Callegary et al., 2007; Lavoue et al., 2010). In fact, testing this approach has shown an average relative error of 5% but a maximum of 300% when compared with simulations using Maxwell-based full solutions; the largest errors are observed in the case of higher EC in the bottom layer and are much larger than what would be expected under conditions of homogeneity (e.g., Figure A1 in McNeill, 1980).

Once the EMI responses are simulated, the evaluation was performed by considering numerous measurement locations, priors, and choices in parameterizations. For all cases shown in this study, the models were evaluated using the misfit function

$$\mathrm{res} = \sum_{i=1}^{n} \left[\left| (\mathrm{dsim}_i - \mathrm{dmes}_i) / \mathrm{dmes}_i \right| \right] / n ,$$

where dmes_i and dsim_i are the logarithms 10 of the measured and simulated EMI data, respectively, and n equals the number of measurements at each location. The acceptance rule to select models for further statistical analysis is a misfit res smaller than 5% as well as no individual misfit (considering each measurement individually) larger than 10%.

Results

We estimated the EC distributions at each location using the developed grid-based search approach and the forward simulated database generated as described above. We explored the obtained EC distributions with increasing levels of constraints in the inversion, including estimation with no, limited, and strong prior constraints.

Parameter Estimation with No Prior Constraints

The subsurface EC distribution was first estimated for the case in which no prior information was available and/or applied. Figure 5a shows the results of one model that was randomly selected among all the accepted models at each measurement location. Figure 5a is simply a more compact way of visualizing numerous accepted simulations at each location (not shown), which yield similar findings with regards to variability and trend along the profile. Thus, the very high lateral variability (from one to the next location) between the EMI models shown in Fig. 5a indicates that numerous and very different models reproduce the EMI data at one location and in its surroundings as well. In fact, most of these models could be obtained with a one-dimensional regularized least-squares-based inversion, depending on the applied parameterization and initial parameter values (e.g., Fig. 4). Figure 5b to 5c show the minimum and maximum values of the EC distributions obtained at each (finely discretized) depth interval from all the selected models at each location. These figures reveal a very large difference between the minimum and maximum values, again indicating that numerous and very different models (and EC values at each depth) can

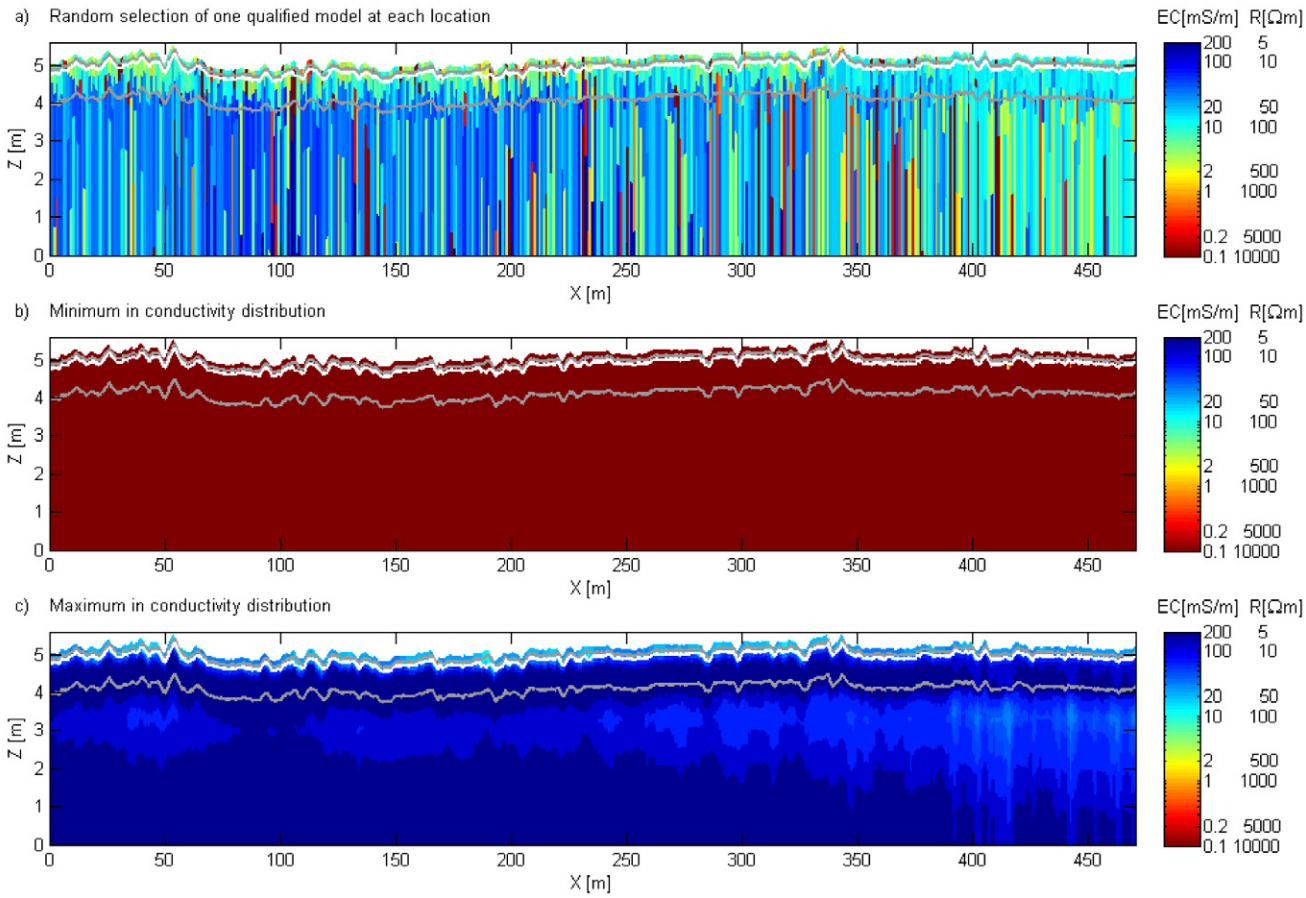

Fig. 5. Parameter-estimation results obtained in case of no prior: (a) random selection of one model among all the accepted models at each location and (b) minimum and (c) maximum EC values observed in all the accepted models at each depth and location. The minimum and maximum depth observed for the boundary between the top and middle layer are indicated by the grey lines and the ones for the boundary between the middle and bottom layer are shown with the white lines (when inside the displayed depth interval). To facilitate visualization, the vertical axis is limited to elevations above 0 m.

reproduce the data within the specified range of uncertainty. Although the non-uniqueness is significant, the lateral variations throughout the profiles (Fig. 5a) show a shallow part that is generally more conductive on the right than the left of the profile, while the deeper part shows the opposite trend. Finally, even if a very low EC for frozen ground (i.e., in the permafrost) were expected below a thin active layer, Fig. 5 suggests that there are many possible EC values in this region if no priors are used in the parameter-estimation approach.

Figure 6 complements Fig. 5 by showing the frequency distribution of both the thickness and EC of each layer at each location. Note that each bin (the interval defined by the black horizontal lines in Fig. 6) of the frequency distribution is related to one of the evaluated parameter values and thus to the same number of initial simulations (i.e., the initial distribution is uniform). The EC distribution in the top layer (Fig. 6a) shows a sharp peak, and its mode is consistent with the EC values observed in the top 0.2 m of the collocated ERT profile (Fig. 2). Further, the top layer EC distributions reveal a very different trend than that observed in the measured apparent EC values (Fig. 3), which highlights the value of using a multidimensional parameter-estimation approach relative to the use of apparent EC for interpretation. Figure 6b to 6e show much flatter and wider distributions for the middle and deeper layers than was revealed by the shallowest layer (Fig. 6a). This suggests that even if the EC of the deeper layers influence the recorded EMI response (Fig. 3), the information within and the variability among the various signals constrain primarily the top layer EC distributions and less significantly the distributions of the deeper layer thickness and EC values (Fig. 6b to 6e).

At each measurement location, the selected models can be investigated in more detail by looking at the five-dimensional solution space defined by the EC of each layer and the thickness of the two upper layers. This is shown in Fig. 7 at 150 and 450 m along the profile, which are two locations that reveal significant differences in terms of subsurface heterogeneity (e.g., Fig. 2 and Fig. 5a). To visualize the five-dimensional solution space, the EC values of the three layers were identified with their three-dimensional coordinates. For each of the combinations, one of the selected

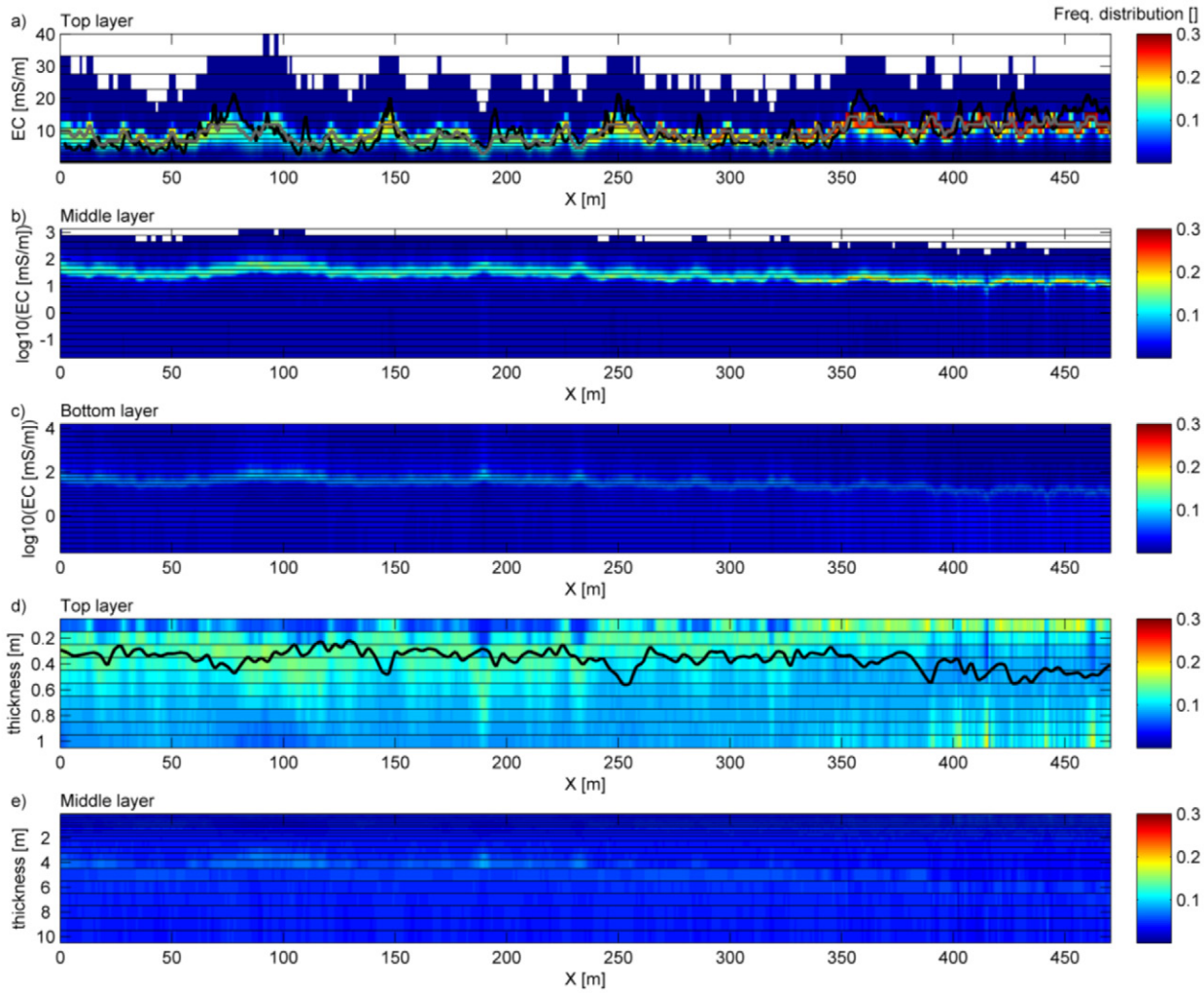

Fig. 6. Frequency distributions of the selected models in the case of no prior: (a) top-, (b) middle-, and (c) bottom-layer EC and (d) top- and (e) middle-layer thickness. In Fig. 6a, the grey line indicates the mode of the distribution and the black line shows the top-layer averaged EC values obtained from the electrical resistance tomography data. In Fig. 6d, the black line indicates the active layer thickness sampled in the field. A frequency value equal to zero is shown in white, the vertical axis is adapted to the minimum and maximum values observed in the selected models, and the color scale has been chosen to be consistent with Fig. 9 and 11.

simulations was then randomly displayed, and the corresponding thicknesses of the top and middle layer were indicated by the size of the symbol and its color, respectively (Fig. 7). In this display, nearby locations that show very different symbol color and size indicate that related parameters can be very diverse and yet still fit the data, while nearby locations that show very limited changes in color and size indicate less variability. This display of the solution domain, which is not possible with standard inversion methods, is very useful for understanding the extent and specificity of solution non-uniqueness in a particular environment. This display also can be used to evaluate the potential effect of priors in reducing the domain of solutions.

Figure 7a shows that the obtained range of EC values for the top layer at 150 m is much more limited than for the other layers (although identical EC values have been evaluated for each layer), indicating again the high information content in the data associated with the top layer relative to the deeper ones. It also shows that if the middle layer were relatively close to the observed apparent EC values (zone between the two black circles), the range of possible EC values for the bottom layer is the largest. In this case, a relatively high bottom-layer EC value (~>35 mS/m) requires the presence of a relatively thick second layer, which will limit the bottom-layer influence on the data. However, if the bottom-layer EC value is relatively low (~<35 mS/m), the top- and second-layer thicknesses can be very diverse and still reproduce the data, because the bottom-layer EC value is about equal or smaller than the second-layer EC value and thus does not significantly constrain the solutions. Further, if the second-layer EC is low compared with the measured apparent EC values (black circle on the left), the EC of the bottom layer has to be high to compensate, while a thicker middle layer leads to higher EC values in the bottom layer. This

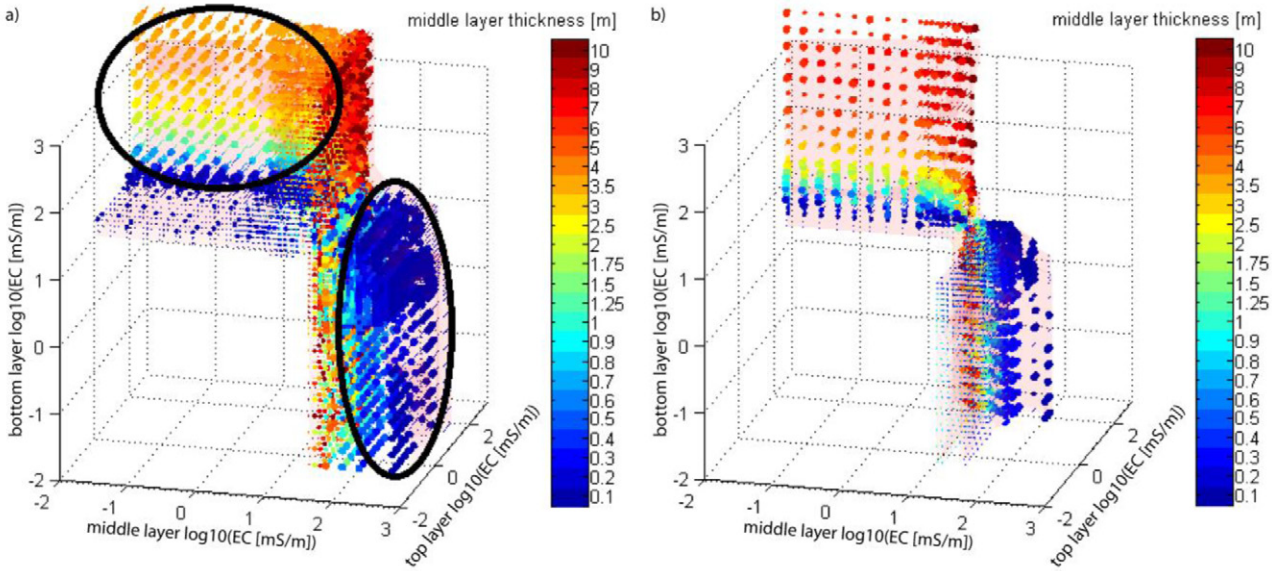

Fig. 7. Multidimensional visualization of the selected models at 150 m (left) and 450 m (right) along the profile. For each combination of three EC values (one per layer), a model was randomly drawn (from the selected corresponding models) and displayed with its top and middle layer thickness shown by the symbol size (larger corresponds to thicker) and color, respectively. Strong local variations in size or color are generally indicative of relatively wide and flat distributions for the corresponding parameter. Interpretations of solutions in circled regions in Fig. 7a are discussed in the text.

equivalence relation is a common issue with the electromagnetic method as described above. Also, in this region (black circle on the left), the maximal thickness of the low EC second layer is ~4 m and the value is not much influenced by the EC variations in the low EC middle layer. In this regard, the true thickness of the low EC second layer is certainly smaller than ~4 m at this location because the bottom-layer maximum EC value evaluated in the grid search (10,000 mS/m or 0.1 Ωm) is extremely large, even for very porous sediment with high-salinity water. Finally, if the second-layer EC is relatively high compared with the measured apparent EC values (black circle on the right of Fig. 7a), its thickness is reduced toward zero because in this case the bottom-layer EC is of very limited influence and thus cannot balance the second-layer EC in the measured apparent EC.

Figure 7b, which shows the solution space at 450 m along the profile, indicates that some trends and behaviors are similar to those observed at 150 m (Fig. 7a). The main difference between the solution domains at the two locations is that given a high EC bottom-layer value, the second layer must be much thicker at 450 m than at 100 m. Also, the selected models are less diverse at 450 m, partly because of the more limited range of possible values for the top-layer EC. Figure 7 clearly emphasizes the need to constrain the bottom-layer EC to estimate the thickness of a low EC middle layer.

Parameter Estimation with Limited and Strong Prior Constraints

We estimated the layer EC distributions using two different sets of constraints on the solution domain by assuming two different states of prior knowledge. We refer to these as cases of "limited" and "strong" prior constraints. For both cases, we used knowledge about EC values of frozen and unfrozen states obtained from previous electrical studies in permafrost systems. We considered models for the selection process only if (i) the top-layer EC was higher than 2 mS/m (<500 Ωm), (ii) the middle-layer EC was lower than 2.85 mS/m (>350 Ωm), (iii) the bottom-layer EC was lower than 250 mS/m (>4 Ωm), and (iv) the top-layer thickness was thicker than 0.2 m and thinner than 0.7 m. The layer thicknesses were limited to a reasonable range of values, based on the active layer thickness measurements performed with a tile probe at the surveyed site as described by Hubbard et al. (2013). The bottom-layer EC distributions were constrained on the basis of the maximum EC values observed over the entire ERT profile (Fig. 2). The strong prior case used additional constraints based on the ERT and point measurements. In this case, additional constraints were invoked by exclusively considering models in which the bottom-layer EC was higher than 47.6 mS/m (<21 Ωm) and the top-layer thickness was within 10 cm from the measured active layer thickness values, which were linearly interpolated along the EMI traverse.

Parameter-estimation results for the limited-prior case are shown in Fig. 8 and Fig. 9. Comparison of Fig. 8a and Fig. 5a indicates that, as expected, the variability between the selected models is more limited than the case in which no priors are used. The range between EC minimum and maximum EC observed in the selected models, which is indicative of variation in the permafrost structure throughout the profile, is also smaller than in the no-prior case. Specifically, the minimum EC observed throughout the profile

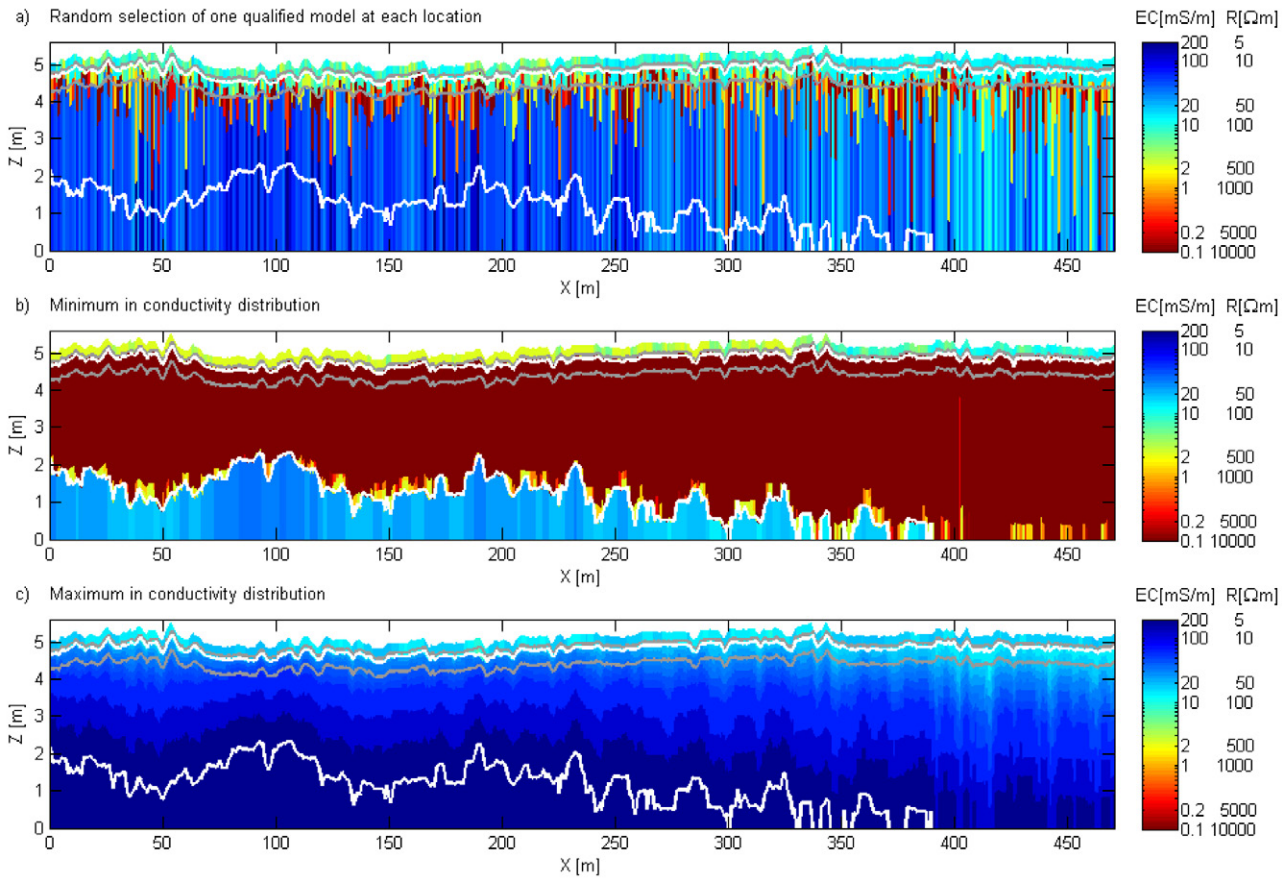

Fig. 8. Parameter-estimation results obtained in case of limited prior: (a) random selection of one model among all the accepted models at each location and (b) minimum and (c) maximum EC values observed in all the accepted models at each depth and location. The minimum and maximum depth observed for the boundary between the top and middle layer are indicated by the grey lines and the ones for the boundary between the middle and bottom layer are shown with the white lines. To facilitate visualization, the vertical axis is limited to elevations above 0 m.

showed a clear EC increase below the observed maximum depth for the second-layer thickness (bottom white line in Fig. 8b). This boundary was the result of enforcing a low EC in the middle layer (which was assumed to be frozen) and limiting the maximum value for bottom-layer EC (based on ERT). With these constraints, the variations in the middle-layer thickness distributions throughout the profile (Fig. 9e) were consistent with the ERT results (Fig. 2). However, the maximum EC values observed in this depth interval (defined by white lines in Fig. 8c) throughout the profile were still generally large relative to the values shown in the ERT data because the bottom-layer EC is not restricted to high EC values and thus allows a large range of models with small second-layer thickness, which would be expected based on Fig. 7.

Figure 9a shows that the defined limited prior helped to reduce the range of the top-layer EC distribution. However, the use of limited-prior information did not significantly change the mode values, which were already consistent with the ERT profile in the no-prior case (Fig. 6a). The constraint applied to the active layer thickness did not improve its estimation; there was no sharp peak in the distributions, and peaks did not correlate well with active layer thickness measured with the tile probe. Similarly, the middle-layer EC values were not predicted more accurately, which is expected because resistive layers are difficult to image since they do not contribute much to the overall response in recorded EMI signal (e.g., McNeill, 1980). Finally, Fig. 9c and 9e show a more variable distribution for bottom-layer EC and middle-layer thickness, respectively, compared with the no-priors case (Fig. 6).

Parameter-estimation results for the case of strong prior constraints are shown in Fig. 10 and Fig. 11. Compared with the no-prior (Fig. 5) and limited-prior cases (Fig. 8), Fig. 10 shows how additional constraints restrict the domain of solutions. Figure 11 indicates that the thickness of the middle layer is now better resolved because of the limited range of possible EC values for the bottom layer. The results correlate well with the general trend observed in the ERT (of an increasing resistive layer thickness from the left to the right of the profile) but still reveal limitations in identifying sharp and very local variations. Although possible reasons for local discrepancies between the EMI and ERT include differences in acquisition, theory, physical processes, and processing of the data, a precise imaging of the thickness of the second layer cannot be expected from

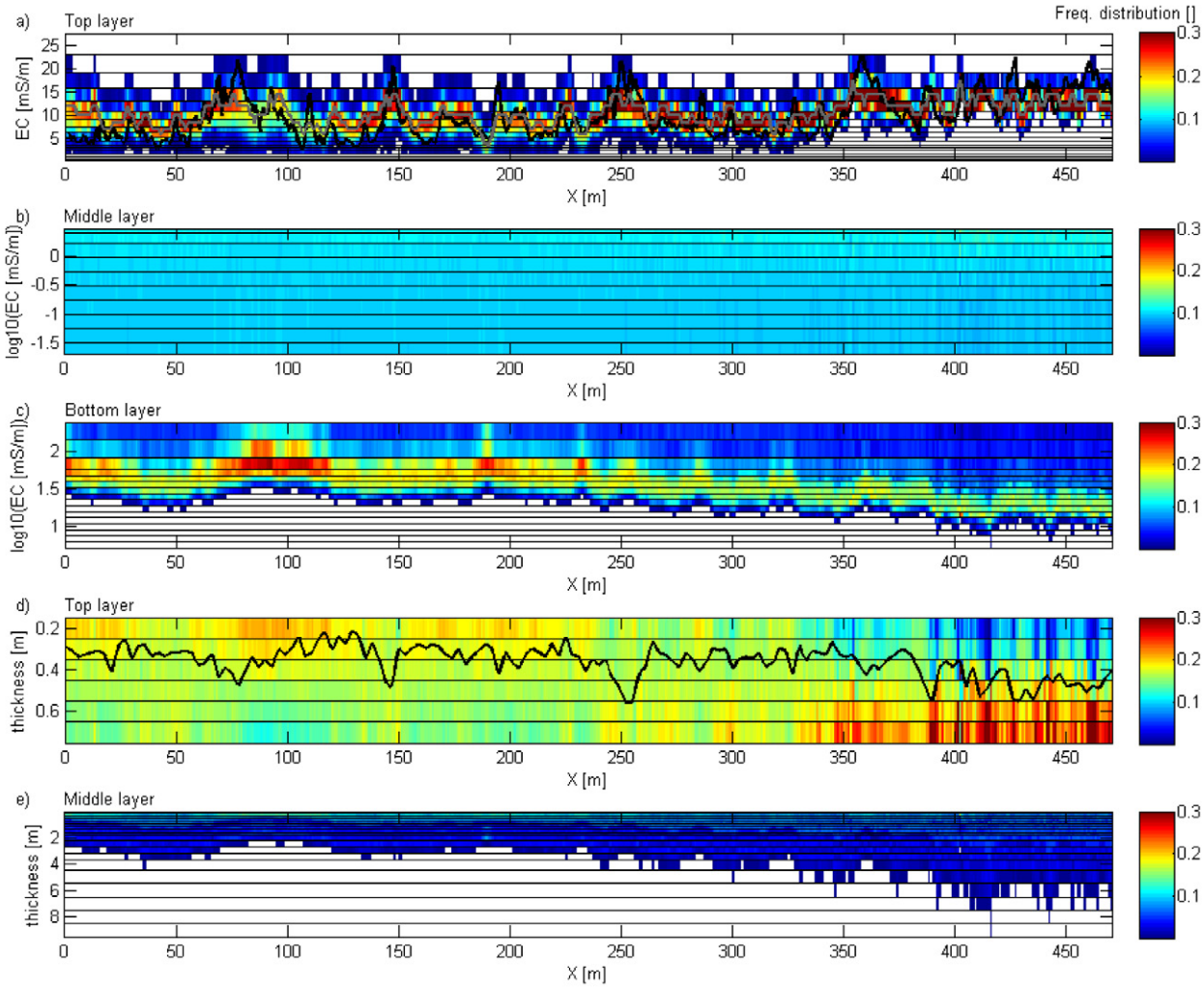

Fig. 9. Frequency distributions of the selected models in the case of limited prior: (a) top-, (b) middle-, and (c) bottom-layer EC and (d) top- and (e) middle-layer thickness. In Fig. 9a, the grey line indicates the mode of the distribution and the black line shows the top-layer averaged EC values obtained from the electrical resistance tomography data. In Fig. 9d, the black line indicates the active layer thickness sampled in the field. A frequency value equal to zero is shown in white, the vertical axis is adapted to the minimum and maximum values observed in the selected models, and the color scale has been chosen to be consistent with Fig. 6 and 11.

such EMI data because of the limited number of measurements and the equivalence principle. Reducing further the observed range of middle-layer thickness values (Fig. 11e) would require stronger constraints on the bottom-layer EC because of the equivalence relation between bottom-layer EC and middle-layer thickness (Fig. 7). Importantly, all the results show that the additional constraints improved the imaging of structural variations below the active layer and reduced the range of observed EC values for the top layer.

Influence of Various Parameterization in the Case of Limited-Prior Constraints

To assess how parameterization choices affect the results, we performed the estimation using the same priors as applied in the case of limited priors (Fig. 8) but with different parameterization choices. We examined the following four subcases: (i) the model acceptance rule was loosened to allow consideration of more models; (ii) some of the measurements at each location were systematically disregarded; (iii) the sampling rate in evaluating the various parameters was decreased; and (iv) the parameter estimation was performed by evaluating two-layered models only.

We first modified the acceptance rule to select models that allow the reproduction of the data with a relative error of maximum 10% instead of the previous 5%. Figure 12 shows that doing this increased the number of selected models and their diversity. Although the width of the top-layer EC distribution also increased compared to the limited-priors case (Fig. 8), the mode of the distribution stayed almost the same (Fig. 12d). In all the other parameter distributions (not shown here), the modes were even more challenging to identify than in the original case of limited priors.

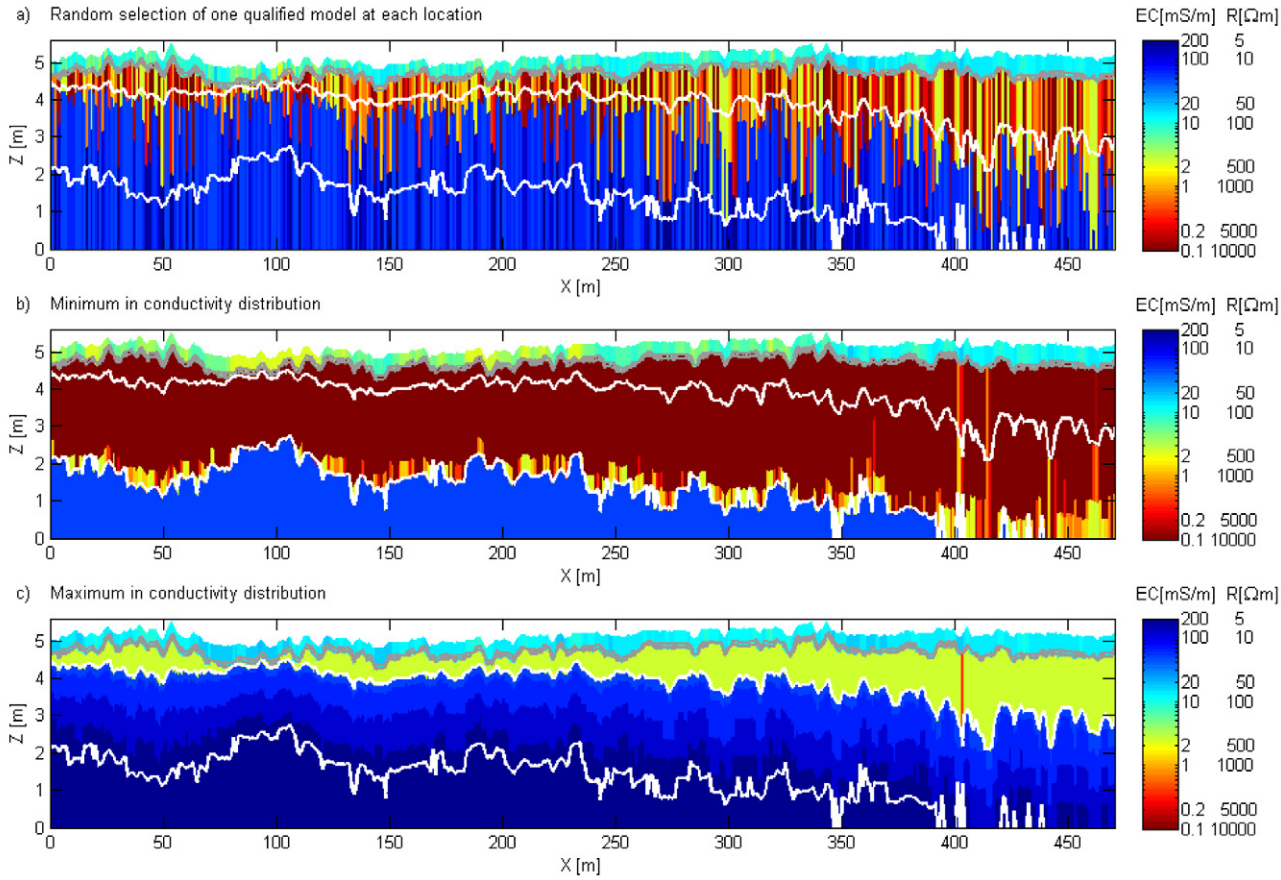

Fig. 10. Parameter-estimation results obtained in case of strong prior: (a) random selection of one model among all the accepted models at each location and (b) minimum and (c) maximum EC values observed in all the accepted models at each depth and location. The minimum and maximum depth observed for the boundary between the top and middle layer are indicated by the closely spaced grey lines and the ones for the boundary between the middle and bottom layer are shown with the white lines. To facilitate visualization, the vertical axis is limited to elevations above 0 m.

For the second subcase, we evaluated the consequences of disregarding some of the measurements at each location. Figure 13 shows the parameter estimation when only the measurements obtained with the vertical configuration of the tool were used (i.e., only half the data previously used, which would take half the time to acquire). In this case, the width of the top-layer EC distribution was significantly increased, but the mode of the distribution did not change substantially (Fig. 13d). This showed that using the tool in the vertical configuration at the Barrow site provides good information about structural variations. In fact, additional tests (not shown) suggested that the 1-m coil spacing in vertical mode provides particularly rich information about the variability below the top layer at the site, while the three other signals provide more information about the top layer. Such assessment is important in developing an efficient survey strategy adapted to the study site characteristics and scientific questions.

For the third subcase, the influence of the number of parameter values evaluated in multidimensional grid was considered by significantly decreasing the sampling rate in each dimension. The coarser grid was obtained by considering only one of two consecutive values in each dimension. In this case, the number of forward simulations was 349,920, which is less than 3.2% of the original ~11 million simulations. The estimated distributions (Fig. 14) show the various effects of using a very coarse grid. In particular, the mode of the top-layer EC distribution and the structure below were estimated less precisely in the presence of a relatively high EC (above ~12.5 mS/m) top layer, as shown by the very sharp change in the EC distributions. Such EC values were too coarsely sampled, as shown by the size of the bins (horizontal black lines in Fig. 14b) and the sharp change from one bin to the next. This subcase suggests that choosing an overly coarse grid can be easily detected and is not critically detrimental to the parameter-estimation results.

For the fourth subcase, we evaluated the consequences of considering two-layered (instead of the previously considered three-layered) models. The parameters evaluated in the multidimensional grid corresponded to the top-layer EC, top-layer thickness, and bottom-layer EC, which required 12,960 forward simulations only. Figure 15 shows the consequences of choosing a two-layered model. First, as expected from the apparent EC measurements (Fig. 3), all two-layered models showed higher EC in the bottom layer (Fig.

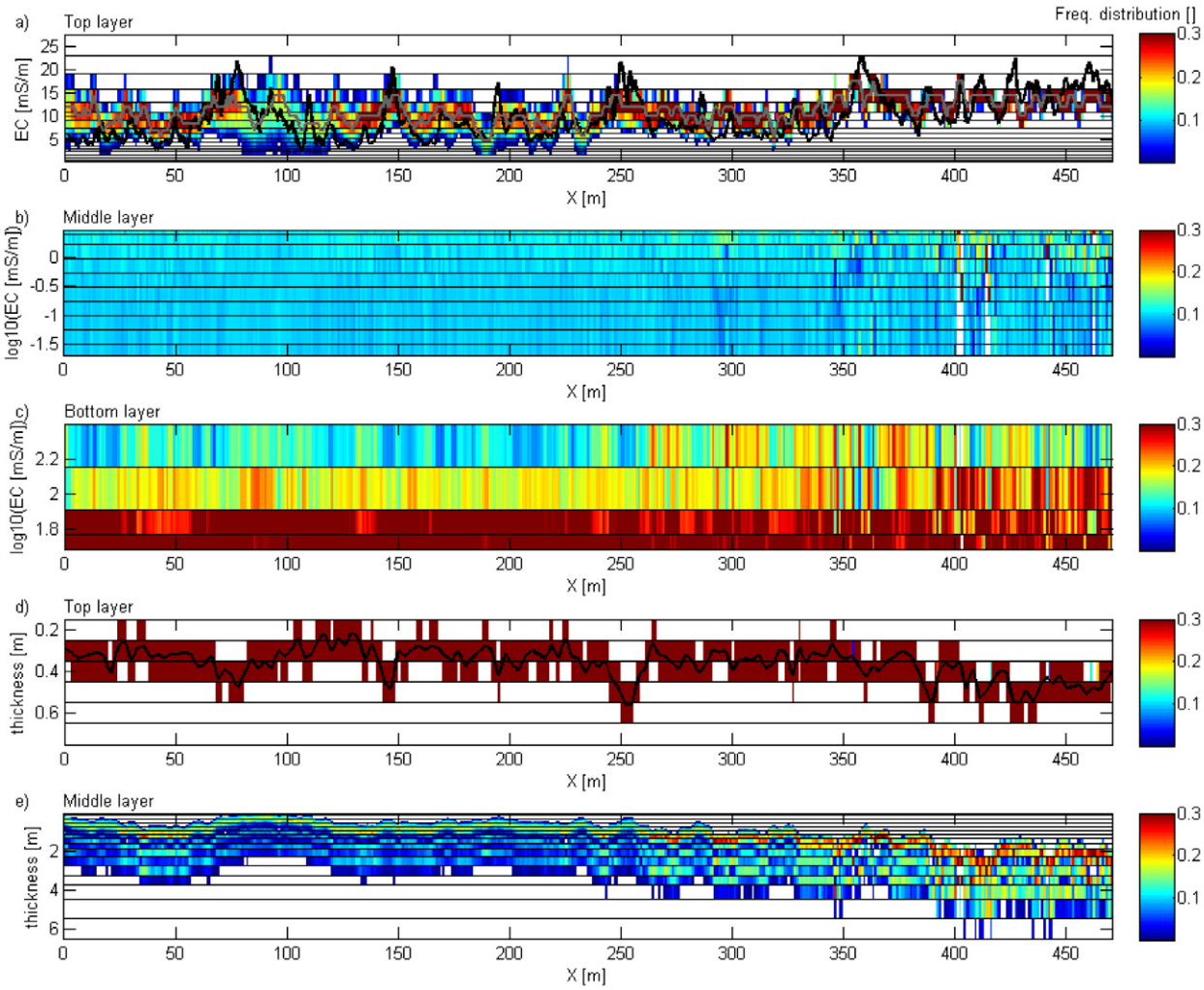

Fig. 11. Frequency distributions of the selected models in the case of strong prior: (a) top-, (b) middle-, and (c) bottom-layer EC and (d) top- and (e) middle-layer thickness. In Fig. 11a, the grey line indicates the mode of the distribution and the black line shows the top-layer averaged EC values obtained from the electrical resistance tomography data. In Fig. 11d, the black line indicates the active layer thickness sampled in the field. A frequency value equal to zero is shown in white, the vertical axis is adapted to the minimum and maximum values observed in the selected models, and the color scale has been chosen to be consistent with Fig. 6 and 9.

15a) and thus failed at imaging the frozen layer visible in the ERT profile (Fig. 2). Second, the mode of the top-layer EC distribution (Fig. 15d) showed higher discrepancies from the EC of the top 0.2 m in the ERT profile, compared with the three-layered model case (Fig. 9a). Although the range of the frequency distribution (i.e., the estimated uncertainty) for both the top-layer EC (Fig. 15d) and the bottom-layer EC (minimum and maximum shown in Fig. 15b and 15c, respectively) was smaller than in the three-layered model case, the two-layered model case led to a much worse estimate of the true subsurface EC distribution. This case study demonstrated that although it was accompanied by greater uncertainty, for this site a three-layer model was more representative of the subsurface.

Discussion and Conclusions

The EMI method is advantageous for characterizing shallow subsurface systems when compared with other methods because large areas can be traversed in a minimum amount of time and in a noninvasive manner. However, it is often challenging to obtain confident estimates in the subsurface EC distributions from EMI datasets because of the non-unique nature of the solution. The objective of this study was to develop a parameter-estimation approach that allows one to quickly evaluate numerous priors and parameterization choices at multiple locations, as well as the influence of these choices on the inferred subsurface models. To this end, we developed and tested a parameter-estimation strategy based on a simple five-dimensional grid-search approach for a three-layer one-dimensional model. The method can easily be

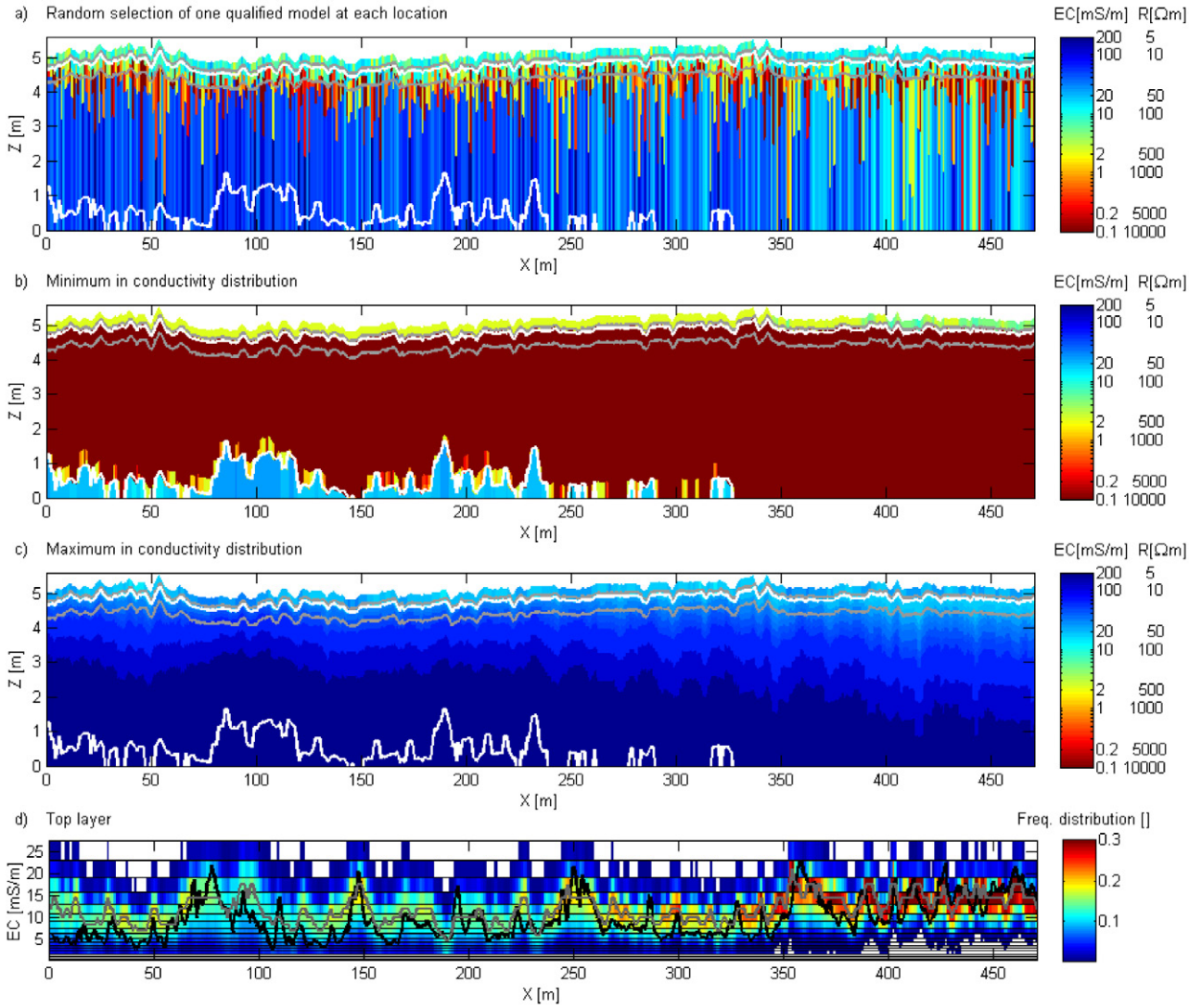

Fig. 12. Parameter-estimation results obtained in the case of limited prior (as Fig. 8) but using an error of 10% instead of 5% for the acceptance rule: (a) random selection of one model amongst all the accepted models at each location, (b) minimum and (c) maximum EC values observed in all the accepted models at each depth and location, and (d) top-layer EC frequency distribution. In Fig. 12a to 12c, the minimum and maximum depth observed for the boundary between the top and middle layer are indicated by the grey line and the ones for the boundary between the middle and bottom layer are shown with the white line. In Fig. 12d, the grey line indicates the mode of the distribution and the black line shows the top-layer averaged EC values obtained from the electrical resistance tomography data.

limited to a two-layered model for use in regions where two layers adequately represents the gross subsurface EC distribution.

This study demonstrated that the developed method is successful at identifying subsurface EC models that reproduce the measured data over a given range of uncertainty. The method is particularly useful for evaluating the information contained in the acquired data, as well as the priors required to constrain the solution, and for applying constraints in a flexible manner to reduce the solution non-uniqueness problem. Importantly, the developed approach permits an adequate exploration and visualization of the solution domain, which can be used to gain an understanding of the extent of non-uniqueness and possible choices for constraining the solution. This is particularly valuable for handling underdetermined problems (i.e., the equivalence issue), which cannot yield a unique solution. Rather than seek a unique solution, the approach investigated the diversity of models that reproduce the data to understand which subsurface information can be reliably extracted from the data. Also, such an understanding is critical for interpreting estimation results and for developing a field acquisition strategy optimized for addressing site-specific scientific questions. Additional advantages of the developed approach include its simplicity (no convergence and optimization required) and the rapidity of investigating the domain of solution and the influence of various priors and measurements. Although this approach required a limited number of investigated dimensions

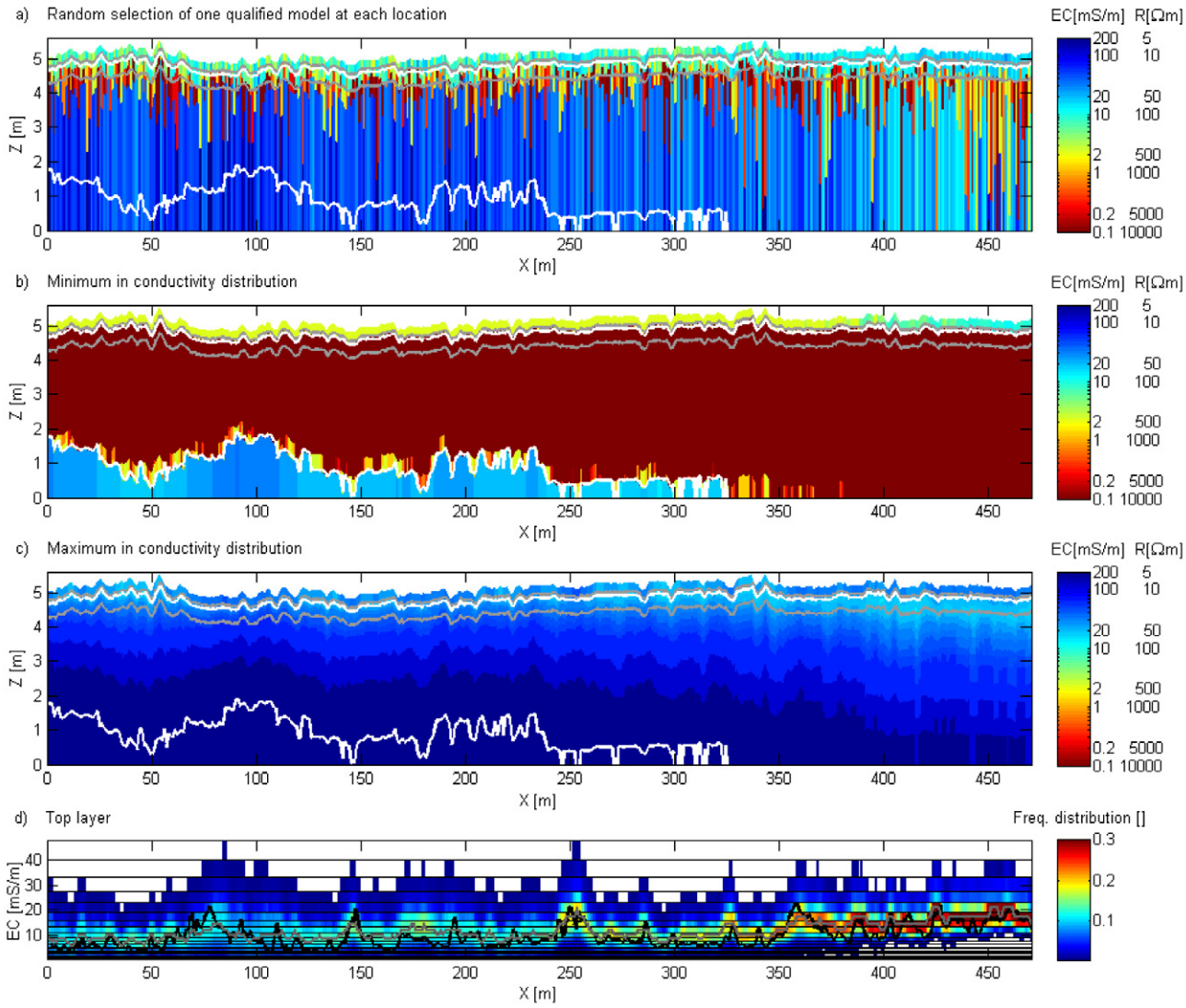

Fig. 13. Parameter-estimation results obtained in the case of limited prior (as Fig. 8) but using only measurement acquired with the EM38 in vertical configuration (half the data): (a) random selection of one model amongst all the accepted models at each location, (b) minimum and (c) maximum EC values observed in all the accepted models at each depth and location, and (d) top-layer EC frequency distribution. In Fig. 13a to 13c, the minimum and maximum depth observed for the boundary between the top and middle layer are indicated by the grey lines and the ones for the boundary between the middle and bottom layer are shown with the white lines. In Fig. 13d, the grey line indicates the mode of the distribution and the black line shows the top-layer averaged EC values obtained from the electrical resistance tomography data.

and parameter values, as well as a fast-running forward modeling code, such simplifications are both pragmatic and often acceptable for a variety of investigations in which the need and influence of priors could be very important.

Application of such an approach to investigate EC distribution from EMI data collected with portable tools has imaged the non-uniqueness in solution and demonstrated the value of reliable priors to estimate parameters such as the thickness of key layers. Thus, improved soil characterization from EMI data can be expected with prior constraints such as knowledge of the site geology, well logging data, core information, and/or additional data. One critical issue with EMI data from portable tools is the calibration of the tool. Although the data assessed here did not show any sign of critical time drift or calibration error, such shifts have been observed in different surveys and studies. Our study results have shown that a measurement uncertainty of about 5% is not unreasonable, given the inherent uncertainty in calibration and drift. Further research will focus on assessing various possible sources of shift in EMI data.

Applying the developed approach to EMI data acquired in an Arctic environment (Barrow, AK) has shown that if no prior constraints are invoked, very diverse subsurface models can reproduce the EMI data. However, even in the case of no priors, the mode of the top-layer EC distribution was evident and consistent with ERT

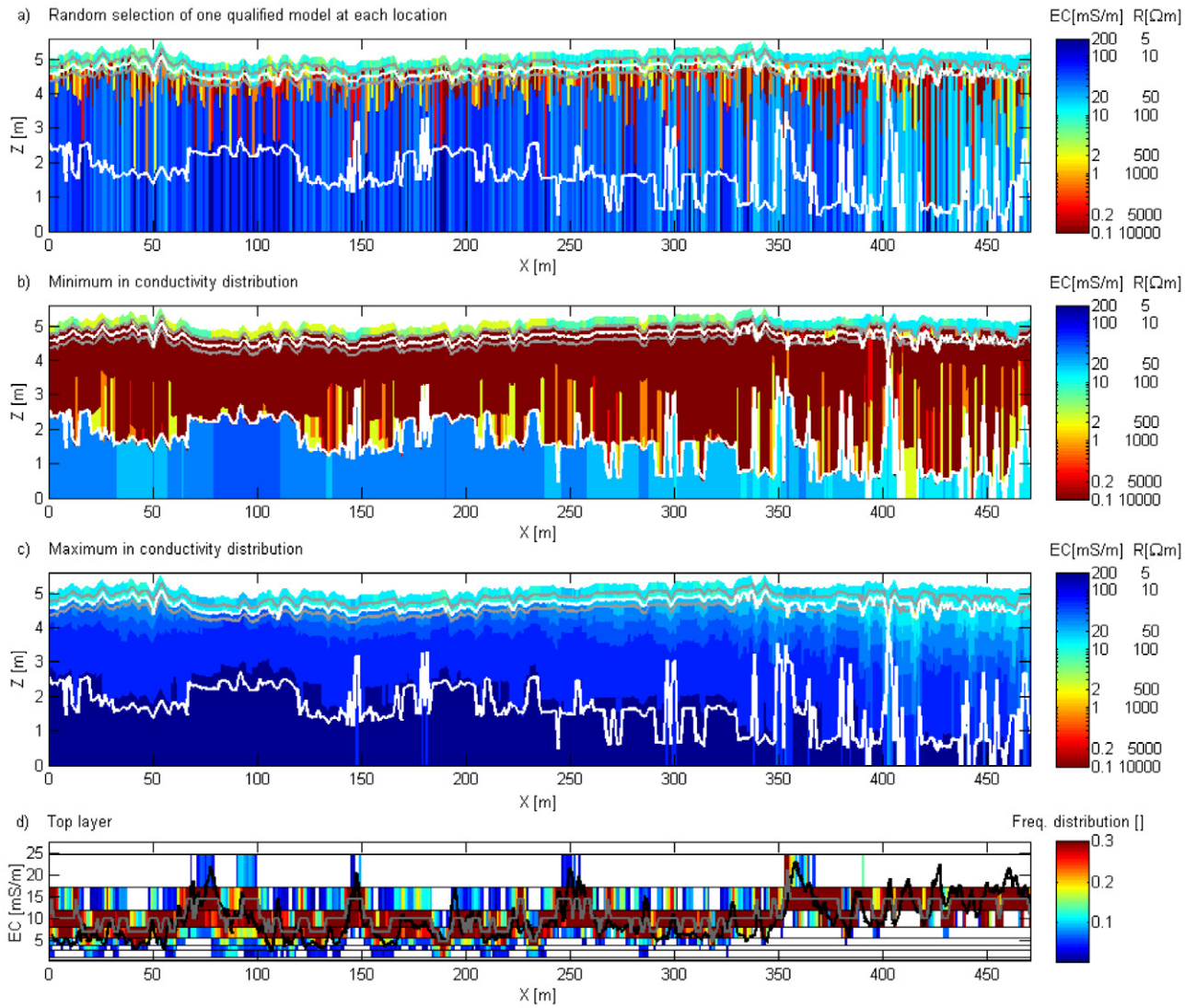

Fig. 14. Parameter-estimation results obtained in the case of limited prior (as Fig. 8) but using a grid of 349,920 models instead of about 11 million: (a) random selection of one model amongst all the accepted models at each location, (b) minimum and (c) maximum EC values observed in all the accepted models at each depth and location, and (d) top-layer EC frequency distribution. In Fig. 14a to 14c, the minimum and maximum depth observed for the boundary between the top and middle layer are indicated by the grey lines and the ones for the boundary between the middle and bottom layer are shown with the white lines. In Fig. 14d, the grey line indicates the mode of the distribution and the black line shows the top-layer averaged EC values obtained from the electrical resistance tomography data.

results. This means that the measured signals contained significant information about the top-layer EC variability, although parameter estimation was required to handle the influence of the various layers. This further suggests that the use of measured apparent EC with point measurements to develop a petrophysical relationship with hydrological properties (as is often performed) can be incorrect. Note that although a 1-m coil spacing antenna in vertical mode (EM38) dictated that the soil below 2-m depth contributed only ~25% of the signal response, this fraction was not negligible. It was particularly non-negligible in the presence of a frozen layer of variable thickness overlying a deeper conductive layer. However, the influence of such structures on the data revealed that they can be characterized at some level by applying site-specific priors.

Applying limited priors reduced the uncertainty in the estimated top-layer EC frequency distribution and constrained estimated parameters to a range of values consistent with the Arctic permafrost environment. Invoking stronger priors based on additional data collected at the site further reduced the uncertainty in estimated parameters and improved the estimation of the second-layer thickness and bottom-layer EC.

Finally, the obtained EC distributions from the EMI data are generally consistent with the collocated ERT profile. Although some local discrepancies exist in imaging deeper structures (likely due to limited related information contained in the EMI data and differences in the physics and processing of both methods), the estimated

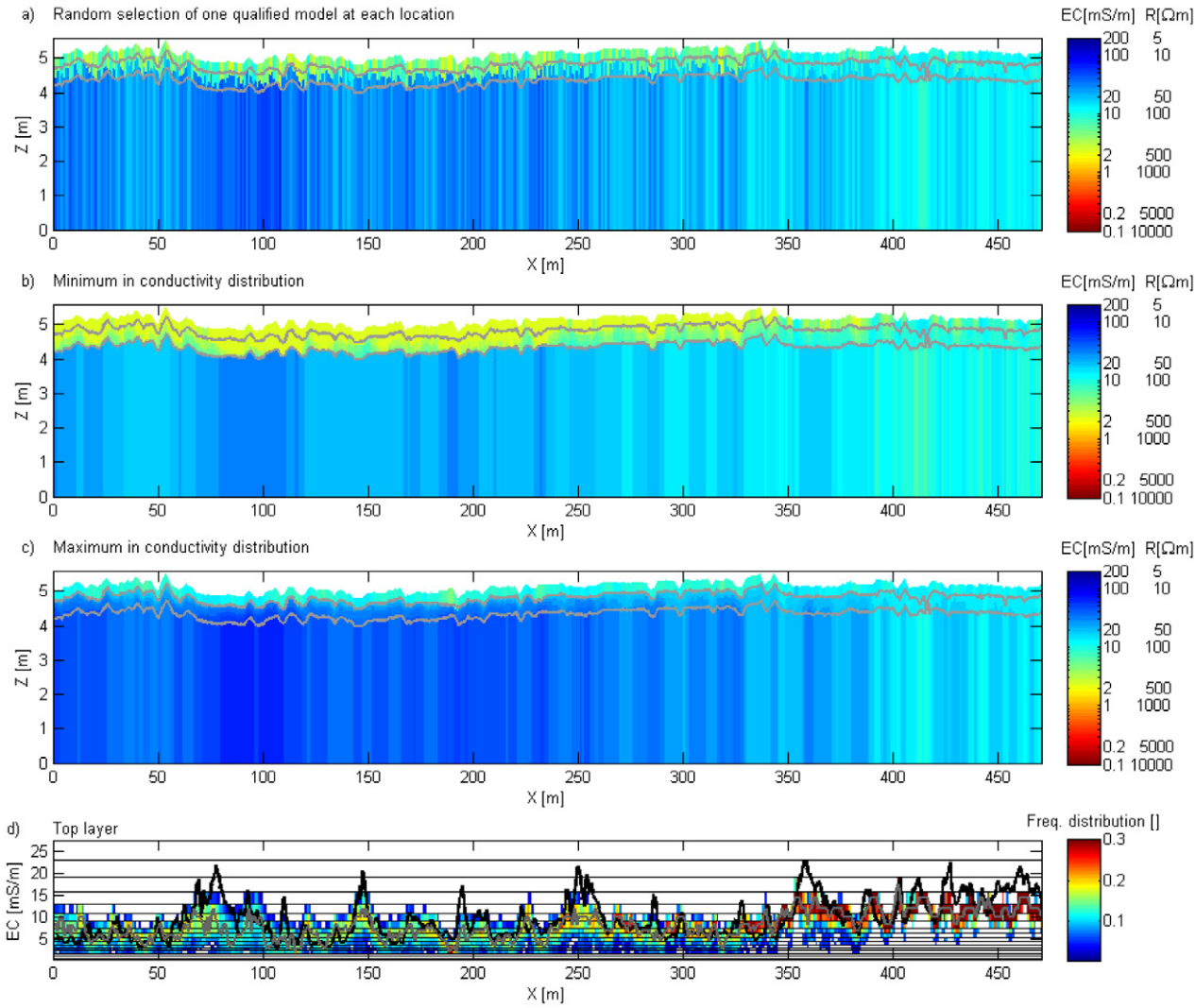

Fig. 15. Parameter-estimation results obtained in the case of limited prior (as Fig. 8) and for a two-layered model case: (a) random selection of one model amongst all the accepted models at each location, (b) minimum and (c) maximum EC values observed in all the accepted models at each depth and location, and (d) top-layer EC frequency distribution. In Fig. 15a to 15c, the minimum and maximum depth observed for the boundary between the top and bottom layer are indicated by the grey lines. In Fig. 15d, the grey line indicates the mode of the distribution and the black line shows the top-layer averaged EC values obtained from the electrical resistance tomography data.

top-layer EC from both methods are very consistent. The results of this study revealed the significant potential of the developed approach and EMI data for depth imaging of larger regions to deliver information relevant for the modeling of carbon cycle in the active layer, and possibly deeper, once the data are interpreted in terms of hydrological or geochemical parameters.

Acknowledgments

The Next-Generation Ecosystem Experiments (NGEE Arctic) project is supported by the Office of Biological and Environmental Research in the DOE Office of Science. This NGEE–Arctic research is supported through contract number DE-AC02-05CH11231 to Lawrence Berkeley National Laboratory. Logistical support in Barrow was provided by UMIAQ, LLC. The authors thank Stan Wullschleger (NGEE–Arctic PI, ORNL) for facilitating our field campaigns, Nigel Quinn (LBNL) for lending us EM38 tools, and Jinsong Chen, Mike Commer (LBNL), and Roman Shekhtman (UBC) for providing codes and guidance for using the EM forward modeling code from LBNL and the University of British Columbia, respectively.

References

Abdu, H., D.A. Robinson, M. Seyfried, and S.B. Jones. 2008. Geophysical imaging of watershed subsurface patterns and prediction of soil texture and water holding capacity. Water Resour. Res. 44:W00D18. doi:10.1029/2008WR007043

André, F., C. van Leeuwen, S. Saussez, R. Van Durmen, P. Bogaert, D. Moghadas, L. de Rességuier, B. Delvaux, H. Vereecken, and S. Lambot. 2012. High-resolution imaging of a vineyard in south of France using ground-penetrating radar, electromagnetic induction and electrical resistivity tomography. J. Appl. Geophys. 78:113–122. doi:10.1016/j.jappgeo.2011.08.002

Archie, G.E. 1945. Electrical resistivity log as an aid in determining some reservoir characteristics. Trans. Am. Inst. Min., Metall. Pet. Eng. 164:322–323.

Auken, E., L. Pellerin, N.B. Christensen, and K. Sorensen. 2006. A survey of current trends in near-surface electrical and electromagnetic methods. Geophysics 71:G249–G260. doi:10.1190/1.2335575

Brown, J. 1969. Ionic concentration gradients in permafrost Barrow, Alaska. U.S. Army Cold Reg. Res. Eng. Lab, Hanover, NH.

Brown, V., M. Hoversten, K. Key, and J. Chen. 2012. Resolution of reservoir scale electrical anisotropy from marine CSEM data. Geophysics 77:E147–E158. doi:10.1190/geo2011-0159.1

Callegary, J.B., T.P.A. Ferre, and R.W. Groom. 2007. Vertical spatial sensitivity and exploration depth of low-induction-number electromagnetic-induction instruments. Vadose Zone J. 6:158–167. doi:10.2136/vzj2006.0120

Cockx, L., G. Ghysels, M. Van Meirvenne, and I. Heyse. 2006. Prospecting frost-wedge pseudomorphs and their polygonal network using the electromagnetic induction sensor EM38DD. Permafrost Periglacial Processes 17:163–168. doi:10.1002/ppp.546

Corwin, D.L., and S.M. Lesch. 2005. Characterizing soil spatial variability with apparent soil electrical conductivity Part II. Case study. Comput. Electron. Agric. 46:135–152. doi:10.1016/j.compag.2004.11.003

Everett, M.E. 2012. Theoretical developments in electromagnetic induction geophysics with selected applications in the near surface. Surv. Geophys. 33:29–63. doi:10.1007/s10712-011-9138-y

Everett, M.E., and M.A. Meju. 2005. Near-surface controlled-source electromagnetic induction: Background and recent advances. In: Y. Rubin and S.S. Hubbard, editors, Hydrogeophysics. Springer, Dordrecht, the Netherlands. p. 157–183.

Farquharson, C.G. 2000. EM1DFM. Univ. of British Columbia Geophys. Inversion Facil., Vancouver, Canada.

Friedman, S.P. 2005. Soil properties influencing apparent electrical conductivity: A review. Comput. Electron. Agric. 46:45–70. doi:10.1016/j.compag.2004.11.001

Frohn, R.C., K.M. Hinkel, and W.R. Eisner. 2005. Satellite remote sensing classification of thaw lakes and drained thaw lake basins on the North Slope of Alaska. Remote Sens. Environ. 97:116–126. doi:10.1016/j.rse.2005.04.022

Geonics. 2009. EM38–MK2 ground conductivity meter operating manual. Geonics, Ontario, Canada.

Goswami, S., J.A. Gamon, and C.E. Tweedie. 2011. Surface hydrology of an arctic ecosystem: Multiscale analysis of a flooding and draining experiment using spectral reflectance. J. Geophys. Res. 116:G00I07. doi:10.1029/2010JG001346

Hauck, C., and C. Kneisel. 2008. Applied geophysics in periglacial environments. Cambridge Univ. Press, Cambridge, UK.

Heil, K., and U. Schmidhalter. 2012. Characterisation of soil texture variability using the apparent soil electrical conductivity at a highly variable site. Comput. Geosci. 39:98–110. doi:10.1016/j.cageo.2011.06.017

Hendrickx, J.M.H., B. Borchers, D.L. Corwin, S.M. Lesch, A.C. Hilgendorf, and J. Schlue. 2002. Inversion of soil conductivity profiles from electromagnetic induction measurements: Theory and experimental verification. Soil Sci. Soc. Am. J. 66:673–685. doi:10.2136/sssaj2002.0673

Hinkel, K.M., J.A. Doolittle, J.G. Bockheim, F.E. Nelson, R. Paetzold, J.M. Kimble, and R. Travis. 2001. Detection of subsurface permafrost features with ground-penetrating radar, Barrow, Alaska. Permafrost Periglacial Processes 12:179–190. doi:10.1002/ppp.369

Hinkel, K.M., W.R. Eisner, J.G. Bockheim, F.E. Nelson, K.M. Peterson, and X.Y. Dai. 2003. Spatial extent, age, and carbon stocks in drained thaw lake basins on the Barrow Peninsula, Alaska. Arct. Antarct. Alp. Res. 35:291–300. doi:10.1657/1523-0430(2003)035[0291:SEAACS]2.0.CO;2

Hoekstra, P., P.V. Sellmann, and A. Delaney. 1975. Ground and airborne resistivity surveys of permafrost near Fairbanks, Alaska. Geophysics 40:641–656. doi:10.1190/1.1440555

Huang, H.P., and I.J. Won. 2003. Real-time resistivity sounding using a handheld broadband electromagnetic sensor. Geophysics 68:1224–1231. doi:10.1190/1.1598114

Hubbard, S.S., C. Gangodagamage, B. Dafflon, H. Wainwright, J. Peterson, A. Gusmeroli, C. Ulrich, Y. Wu, C. Wilson, J. Rowland, C. Tweedie, and S.D. Wullschleger. 2013. Quantifying and relating land-surface and subsurface variability in permafrost environments using LiDAR and surface geophysical datasets. Hydrogeol. J. 21:149–169.

Kafri, U., and M. Goldman. 2005. The use of the time domain electromagnetic method to delineate saline groundwater in granular and carbonate aquifers and to evaluate their porosity. J. Appl. Geophys. 57:167–178. doi:10.1016/j.jappgeo.2004.09.001

Keller, G.V., and F.C. Frischknecht. 1966. Electrical methods in geophysical prospecting. Pergamon Press, Oxford, UK.

Koefoed, O. 1979. Geosounding principles 1: Resistivity sounding measurements. Elsevier Science, Amsterdam.

Lavoue, F., J. van der Kruk, J. Rings, F. Andre, D. Moghadas, J.A. Huisman, S. Lambot, L. Weihermueller, J. Vanderborght, and H. Vereecken. 2010. Electromagnetic induction calibration using apparent electrical conductivity modelling based on electrical resistivity tomography. Near Surface Geophys. 8:553–561.

Leffingwell, E. 1915. Ground-ice wedges, the dominant form of ground-ice on the north coast of Alaska. J. Geol. 23:635–654. doi:10.1086/622281

Lesch, S.M., D.J. Strauss, and J.D. Rhoades. 1995. Spatial prediction of soil-salinity using electromagnetic induction techniques. 2. An efficient spatial sampling algorithm suitable for multiple linear-regression model identification and estimation. Water Resour. Res. 31:387–398. doi:10.1029/94WR02180

McNeill, J.D. 1980. Electromagnetic terrain conductivity measurement at low induction numbers. Tech. Note TN-6. Geonics, Ontario, Canada.

Mester, A., J. van der Kruk, E. Zimmermann, and H. Vereecken. 2011. Quantitative two-layer conductivity inversion of multi-configuration electromagnetic induction measurements. Vadose Zone J. 10:1319–1330. doi:10.2136/vzj2011.0035

Meyer, H., L. Schirrmeister, A. Andreev, D. Wagner, H.-W. Hubberten, K. Yoshikawa, A. Bobrov, S. Wetterich, T. Opel, E. Kandiano, and J. Brown. 2010. Lateglacial and Holocene isotopic and environmental history of northern coastal Alaska—Results from a buried ice-wedge system at Barrow. Quat. Sci. Rev. 29:3720–3735. doi:10.1016/j.quascirev.2010.08.005

Minsley, B.J. 2011. A trans-dimensional Bayesian Markov chain Monte Carlo algorithm for model assessment using frequency-domain electromagnetic data. Geophys. J. Int. 187:252–272. doi:10.1111/j.1365-246X.2011.05165.x

Minsley, B.J., J.D. Abraham, B.D. Smith, J.C. Cannia, C.I. Voss, M.T. Jorgenson, M.A. Walvoord, B.K. Wylie, L. Anderson, L.B. Ball, M. Deszcz-Pan, T.P. Wellman, and T.A. Ager. 2012a. Airborne electromagnetic imaging of discontinuous permafrost. Geophys. Res. Lett. 39:L02503. doi:10.1029/2011GL050079

Minsley, B.J., B.D. Smith, R. Hammack, J.I. Sams, and G. Veloski. 2012b. Calibration and filtering strategies for frequency domain electromagnetic data. J. Appl. Geophys. 80:56–66. doi:10.1016/j.jappgeo.2012.01.008

Mitsuhata, Y., T. Uchida, K. Matsuo, A. Marui, and K. Kusunose. 2006. Various-scale electromagnetic investigations of high-salinity zones in a coastal plain. Geophysics 71:B167–B173. doi:10.1190/1.2335658

Monteiro Santos, F.A. 2004. 1-D laterally constrained inversion of EM34 profiling data. J. Appl. Geophys. 56:123–134. doi:10.1016/j.jappgeo.2004.04.005

Monteiro Santos, F.A., J. Triantafilis, and K. Bruzgulis. 2011. A spatially constrained 1D inversion algorithm for quasi-3D conductivity imaging: Application to DUALEM-421 data collected in a riverine plain. Geophysics 76:B43–B53. doi:10.1190/1.3537834

Overduin, P.P., S. Westermann, K. Yoshikawa, T. Haberlau, V. Romanovsky, and S. Wetterich. 2012. Geoelectric observations of the degradation of nearshore submarine permafrost at Barrow (Alaskan Beaufort Sea). J. Geophys. Res. 117:F02004. doi:10.1029/2011JF002088

Pellerin, L. 2002. Applications of electrical and electromagnetic methods for environmental and geotechnical investigations. Surv. Geophys. 23:101–132. doi:10.1023/A:1015044200567

Quinn, N.W.T., R. Ortega, P.J.A. Rahilly, and C.W. Royer. 2010. Use of environmental sensors and sensor networks to develop water and salinity budgets for seasonal wetland real-time water quality management. Environ. Model. Software 25:1045–1058. doi:10.1016/j.envsoft.2009.10.011

Reedy, R.C., and B.R. Scanlon. 2003. Soil water content monitoring using electromagnetic induction. J. Geotech. Geoenviron. Eng. 129:1028–1039. doi:10.1061/(ASCE)1090-0241(2003)129:11(1028)

Revil, A., L.M. Cathles, S. Losh, and J.A. Nunn. 1998. Electrical conductivity in shaly sands with geophysical applications. J. Geophys. Res. 103(B10):23,925–23,936. doi:10.1029/98JB02125

Robinson, D.A., H. Abdu, I. Lebron, and S.B. Jones. 2012. Imaging of hill-slope soil moisture wetting patterns in a semi-arid oak savanna catchment using time-lapse electromagnetic induction. J. Hydrol. 416–417:39–49. doi:10.1016/j.jhydrol.2011.11.034

Sellmann, P.V., J. Brown, R.I. Lewellen, H. McKim, and C. Merry. 1975. The classification and geomorphic implication of thaw lakes on the Arctic Coastal Plain, Alaska. CRREL Res. Rep. 344. U.S. Army Cold Reg. Res. Eng. Lab, Hanover, NH.

Sen, M., and P.L. Stoffa. 1995. Global optimization methods in geophysical inversion. Elsevier, Amsterdam.

Sharma, S.P., and P. Kaikkonen. 1999. Appraisal of equivalence and suppression problems in 1D EM and DC measurements using global optimization and joint inversion. Geophys. Prospect. 47:219–249. doi:10.1046/j.1365-2478.1999.00121.x

Shiklomanov, N.I., D.A. Streletskiy, F.E. Nelson, R.D. Hollister, V.E. Romanovsky, C.E. Tweedie, J.G. Bockheim, and J. Brown. 2010. Decadal variations of active-layer thickness in moisture-controlled landscapes, Barrow, Alaska. J. Geophys. Res. 115:G00I04. doi:10.1029/2009JG001248

Singleton, A.C., G.R. Osinski, C. Samson, M.-C. Williamson, and S. Holladay. 2010. Electromagnetic characterization of polar ice-wedge polygons: Implications for periglacial studies on Mars and Earth. Planet. Space Sci. 58:472–481. doi:10.1016/j.pss.2009.09.013

Tarantola, A. 2005. Inverse problem theory and methods for model parameter estimation. SIAM, Philadelphia, PA.

Triantafilis, J., and S.M. Lesch. 2005. Mapping clay content variation using electromagnetic induction techniques. Comput. Electron. Agric. 46:203–237. doi:10.1016/j.compag.2004.11.006

Triantafilis, J., and F.A. Monteiro Santos. 2009. 2-Dimensional soil and vadose-zone representation using an EM38 and EM34 and a laterally constrained inversion model. Aust. J. Soil Res. 47:809–820. doi:10.1071/SR09013

Triantafilis, J., J.A.E. Roe, and F.A. Monteiro Santos. 2011. Detecting a leachate plume in an aeolian sand landscape using a DUALEM-421 induction probe to measure electrical conductivity followed by inversion modelling. Soil Use Manage. 27:357–366.

Ward, S.H., and G.W. Hohmann. 1987. Electromagnetic theory for geophysical applications. In: M.N. Nabighian, editor, Electromagnetic methods in applied geophysics. Vol. 1. Soc. of Explor. Geophysicists, Tulsa, OK. p. 131–311.

Yoshikawa, K., V. Romanovsky, N. Duxbury, J. Brown, and A. Tsapin. 2004. The use of geophysical methods to discriminate between brine layers and freshwater taliks in permafrost regions. J. Glaciol. Geocryology 26:301–309.